Materials and Processing for Wearable Healthcare Electronics Systems: Flexible Circuit Boards and Stretchable e-Textile Patches for Surface Electromyography

by

Shide Qiu

A thesis submitted in partial fulfillment of the requirements for the degree of

Master of Science
in

MATERIALS ENGINEERING

Department of Chemical and Materials Engineering
University of Alberta

Abstract

Skin-adhesive electrodes – more preferably, integrated electronic systems with embedded signal processing and transmittance – that can be worn comfortably on a patient have irreplaceable importance in healthcare. For example, surface electromyography (sEMG) is a non-invasive electrodiagnostic medical technique to detect, record, and interpret electric activity of groups of muscles from skin surface right above them. If skin-adhesive sEMG electrodes can be integrated with wireless data processing and transmittance system in a compact and wearable format, these devices can provide unprecedented opportunities for applications such as posture monitoring for rehab medicine, swallowing self-coaching, and muscle fatigue detector. However, there are stringent demands for form factors that are specific for the target locations in body, such as required level of flexibility, foldability and stretchability. The conversion of electronics into such advanced form factors has been arising the current challenges in the skin-adhesive electronic systems, such as poor reusability, complicated fabrication methods, and poor connection between soft and hard components in the electronics system. In this thesis, we have explored the potential solutions to solve these problems.

Overall, this thesis is divided into two themes. In the first theme, we developed a versatile technology with capability of rapid, simple, customizable fabrication of flexible printed circuit boards (Flex-PCBs) and sensors. A simple and cost-effective wax-printing technique to pattern flexible interconnects allowed the system-level integration of sensing, processing, power, and wireless communication units. The flexible circuitry with reusable adhesive can follow the contour of curvilinear skin topology, thus allow enhanced wearability for skin-adhesive electronic systems.

In the second theme, we developed textile-based electronics, also known as 'e-textiles', which offer stretchability and comfort for patients. A stretchable conductive silver ink was developed for ink-jet printing to pattern stretchable circuits on nano-textiles. The deep permeation of ink into nano-textiles resulted in stable adhesion, mechanically and electrically strengthen. With our custom-developed electronic circuits, we demonstrated a sEMG system with wireless data emission.

Key words: flexible and stretchable electronics, wearable healthcare devices, printed electronics, hard/soft material integration, surface electromyography (sEMG)

Preface

(Mandatory due to collaborative work)

This thesis is organized in five chapters.

Chapter 1 is the introduction.

Chapter 2 is the background.

Theme 1 (flexible electronics) consists of Chapter 3.

Chapter 3 of this thesis will be further refined and be prepared for a journal submission as T.-G. La, S. Qiu, D. K. Scott, J. Rieger, H.-J. Chung, "Flexible, Multilayered Printed Circuit Boards and Sensors for Surface Electromyogram". T.-G. La, S. Qiu, and H.-J. Chung conceived the idea. S. Qiu and T.-G. La performed the experiments and carried out data interpretation. D. K. Scott designed the electronic circuits.

Theme 2 (stretchable e-textiles) consists of Chapters 4 and 5.

Some parts of Chapter 4 in this thesis is currently in-press for publication in *Advanced Healthcare Materials* as T.-G. La, S. Qiu, D. K. Scott, R. Bakhtiari, J. W. P. Kuziek, K. E. Mathewson, J. Rieger, H.-J. Chung, "Two-Layered and Stretchable e-Textile Patches for Wearable Healthcare Electronics". T.-G. La and S. Qiu contributed equally to this work. S. Qiu, T.-G. La, and H.-J. Chung conceived the idea. S. Qiu and T.-G. La performed the experiments and carried out data interpretation. D. K. Scott and R. Bakhtiari designed the electronic circuits. J. W. P. Kuziek, K. E. Mathewson measured and interpreted EEG data. S. Qiu and T.-G. La wrote the manuscript with iterated revisions and instructions from H.-J. Chung, followed by revisions and edits by all authors.

Chapter 5 of this thesis has been prepared for submission as S. Qiu, T.-G. La, L. Zheng, A, Elias, J. Rieger, H.-J. Chung, “Stretchable, Mechanically and Electrically Robust E-Textiles by Controlling Ink Permeation and Nano-Fiber Encapsulation”. S. Qiu, T.-G. La, and H.-J. Chung conceived the idea. S. Qiu performed the experiments with the help of T.-G. La. Data interpretation was carried out under the guidance of T.-G. La and H.-J. Chung. L. Zheng conceptualized and designed cartoons. S. Qiu wrote the manuscript with iterated revisions and instructions from H.-J. Chung, followed by revisions and edits by A. Elias and J. Rieger.

The overall conclusions of the thesis are summarized in Chapter 6.

Acknowledgements

First and foremost, I would like to thank my supervisor, Dr. Hyun-Joong Chung for his continuous support and encouragement during my master study at the University of Alberta. He has always inspired me with his enthusiasm and dedication for research. I deeply appreciate all his advice and supports to make my MSc experience at University of Alberta. I am also very grateful for his patience, inspiration and immerse knowledge in the areas of expertise. I would like to thank Dr. Jana Rieger for her enthusiasm, inspiration and guidance to this project.

I am fortunate to have great labmates during my master's study at University of Alberta. They encouraged and helped me a lot in both academic fields and life and made my two years of life in Canada fulfilling. Specifically, I want to acknowledge Dr. Thanh-Giang La, my mentor, who was ever-present to help me with his expertise in stretchable electronics during this time. I am especially appreciative of Li Liu, Fanghui Liu, Hemant Charaya, Wendy Tran, and Lelin Zheng. Thanks for the help in doing research and above all for precious friendship.

I wish to express my great love and gratitude to my beloved family: To my father, Xingwu Qiu, and my mother, Yuhong Gu, for their endless love, unconditional support, encouragement, and always being there for me.

Shide Qiu

November 2018

Table of Contents

List of Figures

List of Tables

Chapter 1. Introduction

Wearable biosensors, which can monitor heart rate, wrist pulse, body temperature, and sweat bio-information, provide unprecedented opportunities for personal portable devices with remote medicine practices. Their ability to transmit data to doctors in remote locations and get real-time feedback are expected to revolutionize healthcare, decrease the overall costs of healthcare service, and improve the quality of human life. Currently, wearable healthcare electronics contains rigid power sources and electrical components which limit its ability to stretch and bend[1, 2]. Thus, flexible and stretchable interconnects are critical as they can provide rigid electronics an extra degree of flexibility and stretchability and can be attached to various curvilinear parts of human bodies.

1.1 Surface EMG

Wearable devices can be worn directly on differently parts of body. The wearable devices for health monitoring create new opportunities for personal portable devices with remote medicine practices. Multi-functional flexible electronics are essential to health monitoring systems with the abilities of real-time sensing of physiological signals. Collecting these physiological signals can provide continuous and non-invasive health diagnosis and assessments[3-6].

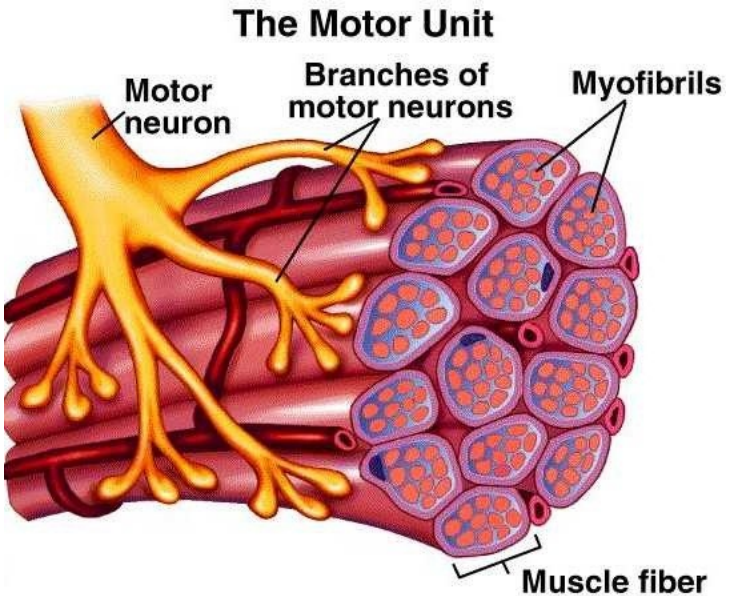

Figure 1.1. A motor unit consists on one motor neuron and all the muscle fibers it stimulates. Reproduced with permission from [7].

Electromyogram (EMG) is a technique for detecting and analyzing electrical signals produced by skeletal muscles. The electrical signal emanated from muscle activation is the myoelectric signal which is produced from small electrical currents generated by the exchange of ions across the muscle membranes[7]. As shown in Fig. 1.1, a motor unit is the junction point where the motor neuron and muscle fibers meet. After the action stimulus is transmitted across the neuromuscular junction, an action potential is elicited in all the innervated muscle fibers of that particular motor unit to produce the resultant EMG signals[8]. Moreover, more motor units will be activated to achieve high EMG signal amplitudes when greater force is generated[9].

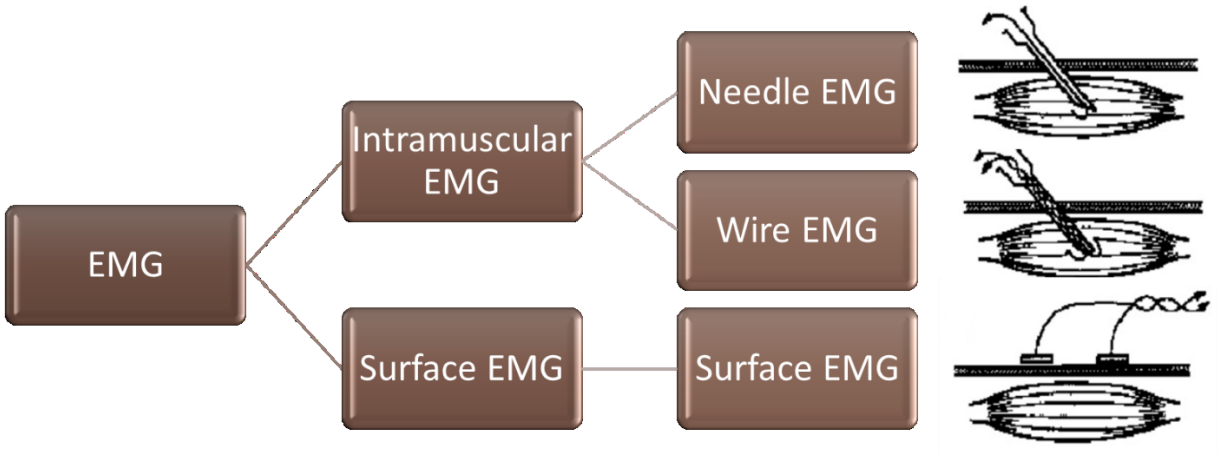

Figure 1.2. Classification of most widely used EMG electrodes. Reproduced with permission from [7]

Nowadays, there are two main types of EMG devices: surface EMG (sEMG) and intramuscular EMG as shown in Fig. 1.2. For intramuscular EMG, needle electrode and wire electrode are two different types of electrodes. Needle electrodes are widely used in clinical and their electrode tips are bare. Wire electrodes are usually made from small diameter, highly non-oxidizing and stiff wire with insulation[9]. However, both needle and wire electrodes will cause extra pain and inconvenience because they need to be inserted through the skin into the muscle tissue during the measurement. Thus, more people are interested in sEMG electrodes which can provide a non-invasive measurement to detect EMG signals. It also achieves daily use with minimum medical supervision for public patients. For example, head and neck cancer treatment alters the anatomy and physiology of patients. Resulting swallowing difficulties can lead to serious health concerns, such as malnutrition, dehydration, and aspiration pneumonia. A sEMG device can be used as a visual biofeedback adjuvant to swallow therapy, guiding the patient to perform the exercise correctly. However, there are still several limitations that need to be solved.

Most commercial sEMG devices cannot be conformable with curvilinear surface of the skin or perform good connection between skin surface and electrodes. Moreover, commercial sEMG devices need messy wires and bulky circuit boards to measure the signal, causing difficulties of wearing the device daily. Thus, a conformable and comfortable sEMG device is highly demanded.

Recently, textile-based electronics (e-textiles) attract a lot of attentions due to their unique characteristics including softness, thermal dissipation, breathability, light weight, and high conformability. Moreover, embedding electronics in textiles has been suggested to be a next-generation technology. For personalized healthcare devices, an ultimate user comfort would be achieved with e-textiles.[10-12]. In recent years, the use of e-textiles has shown tangible outcomes with the aid of advanced nanotechnologies.[13-18] A complete form of fully integrated e-textile systems include semiconducting transistors,[19, 20] processing units,[21, 22] sensors,[23-28] generators,[29-33] and energy storage units.[34, 35]

To achieve a fully integrated e-textile, stretchable interconnects (sometimes referred as conducting traces) are central to the seamless integration of functional devices with the desirable mechanical properties of the substrate textiles. In the last decade, such conducting traces in smart e-textiles have been realized either (i) by interweaving metallic or polymeric 1D thread conductors into textiles,[36, 37] (ii) by fully coating 2D textile sheets with conductive materials,[38] or (iii) by patterning or printing the traces on 2D textile/fabric substrates.[17, 29, 39, 40] Strategy (i) has been challenged by the limited material selection of the electronic threads. Strategy (ii) suffers from the lack of deterministic pattern ability, thus miniaturization is not a straightforward task. Strategy (iii) is currently prevailing in a large spectrum of applications with the aid of recent advances in materials and printing techniques. Recently, Someya and co-workers achieved screen

printable viscous composite inks to have a low surface resistivity of 0.06 Ωsq^{-1} by processing a multi-layered print (5 overlays) under pressing (30 kPa) and at high temperature (160 ºC); this technique produced an e-textile capable of mechanically withstanding cyclic stretching (1000 cycles at 10% maximum strain) with a resulting order of magnitude increase in electrical resistance.[40, 41] A drawback of the process may be the involvement of hot-press processing, which may cause a thermally induced degradation of textile properties as most commodity textiles degrade at temperatures between 125 ºC and 180 ºC.[42]

In our work, we develop a stretchable, mechanically and electrically robust e-textile sensory patch with integrated electronic system for sEMG applications. Here, silver-based fluoroelastomer ink forms conducting traces via ink-jet printing at room temperature. The permeated composite ink forms a cladding onto the nanofibers in the textile substrate, which is beneficial for mechanical and electrical properties of the e-textile. The printed e-textiles feature conductivity of ~3200 Scm^{-1} with high stretchability and durability over repeated strain cycles. Finally, a sEMG system with wireless data transmission is demonstrated with our e-textile based systems.

1.2. Scope of the Thesis

This thesis focused on the direction of developing wearable bioelectronics within simple and cost-effective techniques. In this work, we fabricated flexible and stretchable surface electromyography (sEMG) monitoring device using two different printing techniques. Firstly, a simple and cost-effective wax-printing technique was developed for flexible wearable devices. Secondly, we developed a stretchable, mechanically and electrically robust e-textile by directly printing stretchable and textile-permeable silver ink on top of polyurethane-based nano-textile substrate.

Chapter 2 is the background.

Chapter 3 of this thesis covers the development of wax-printing technique, the durability of wax-printed flexible circuits, and the electrical integrated sEMG circuit for health monitoring.

In Chapter 4, we developed a fully printed two-layered e-textile system. We further used the e-textile system to make a sEMG system for monitoring muscles activities.

In Chapter 5, we further investigated the property of the ink developed in Chapter 4. We realized a mechanically strengthened and electrically stable e-textile by adjusting the permeation of the stretchable silver ink in the nano-textile. This is done by selecting certain solvent to swell the polyurethane-based nano-textle. Meanwhile, the silver particles encapsulating nano-fibers (cladded-layer) result in mechanically and electrically strengthened e-textile.

The overall conclusions of the thesis are summarized in Chapter 6.

Chapter 2. Background

2.1. Review of Printing Techniques

In recent years, printing technologies are growing rapidly in flexible and stretchable electronics field due to their attractive features such as low fabrication cost and simple fabrication process[43]. Such printing technologies include microcontact printing, transfer printing, spray coating, screen printing and ink-jet printing. They are more preferable in manufacturing due to their low cost and fast processing speed in comparison to photolithography[43]. Specifically, photolithography is the standard method of printed circuit board and microprocessor fabrication[44]. It begins with a clean silicon wafer spincoated with photoresist. A photomask with defined pattern is aligned precisely on top of the photoresist layer. Then the UV light is passed through the photomask onto the photoresist layer. The exposed areas cause a certain chemical reaction leaving the light-sensitive material more soluble. Then it can be removed easily and leave the pattern that was originally under the mask. Metal layer is sputtered or evaporated onto the surface. Finally, photoresist is removed, leaving behind precisely deposited features. However, its main disadvantage is that it requires cleanroom facility to offer extremely particle-free fabrication conditions and expensive specialized equipments [45]. Also, every each pattern requires a unique photomask with certain designed pattern, which is not cost-effective for personalized product designs, which are much required for biomedical applications [46].

For printing technologies, microcontact printing uses a pre-fabricated stamp to take the conductive ink and then contact with the target substrate under specific pressure[47]. The stamp can be repeatably used while it may overtake some ink easily with overload pressure resulting in poor resolution of the printed structure. Conventional microcontact printing can reach a

resolution of ~ 100 μm[47]. For the transfer printing, the desired feature is first digitally printed on special heat transfer paper using a solvent ink. the ink allows the feature to be transferred from the paper to the target substrate with certain press and heat. The resolution of transfer printing can reach 30 μm[48-51]. However, it always requires high temperature and pressure condition. Also, only very limited ink (the one can be sublimated under heat) can be used for it. Spray coating is another popular printing technique. It is always used in combination with other printing technologies such as stamp printing. It utilizes a nozzle to spray solution-based ink on the stamp surface with certain feature. The coated stamp is then contacted with the target substrate to print the desired feature[52]. Such technique has efficient material usage [53]. However, the tensile bond strength achieved by spray coating is low in comparison to other coating processes. Also, spray coatings are anisotropic. In other words, their tensile strength is 10 times higher in longitudinal direction than in the direction parallel to the spray[54]. As for screen printing, it uses a solution-based or colloid-based ink which is more viscous in comparison to spray coating. The basic set up of screen printing is a stencil, squeegee, a press bed and the substrate. The resolution is limited by several factors including mesh size of the stencil, viscosity of the ink and the speed of the printing[55, 56]. The main disadvantage of screen printing is that one stencil can only be used for one pattern design which is not cost-effective. Currently, screen printing technique can reach the highest resolution of 50 μm[57]. Compared to screen printing, ink-jet printing can realize a versatile pattern directly from graphical designs. The resolution is mainly dependent on the parameters of the printing nozzle[58, 59]. Table 1 compares the resolution of each printing method.

Table 1. Comparison of resolution for different printing technologies

Printing method	Resolution	Reference
Microcontact printing	~100 μm	[47]
Transfer printing	~30 μm	[48-51]
Spray printing	~100 μm	[52]
Screen printing	~ 50 μm	[57]
Ink-jet printing	~ 20 μm	[60]

2.2. Our Jet Printing Method

nScrypt 3Dn tabletop printer with its SmartPump^{TM} technology and a high-precision computer-controlled valve can dispense precise starts and stops and handle an extreme range of material viscosities (1-1,000,000 cps)[60]. It can accurately print line width as small as 20μm onto different substrate materials. The printing designs are created by PCAD software and the dispensing parameters including pressure, valve opening, dispensing height, and printing rate are controlled by the computer software. The dispensing pump is shown in Fig. 2.1 which consists of a dispensing valve, pressurized flow inlet, and dispensing tip[61]. During the printing process, a constant positive pressure is applied to the tip chamber from the pressurized flow inlet to push the material out of the dispensing tip. The suck-back function is embedded in the SmartPump^{TM} which can provide a negative pressure in the closing process to suck back the material into the dispensing nozzle to achieve a clean stop and a fresh start.

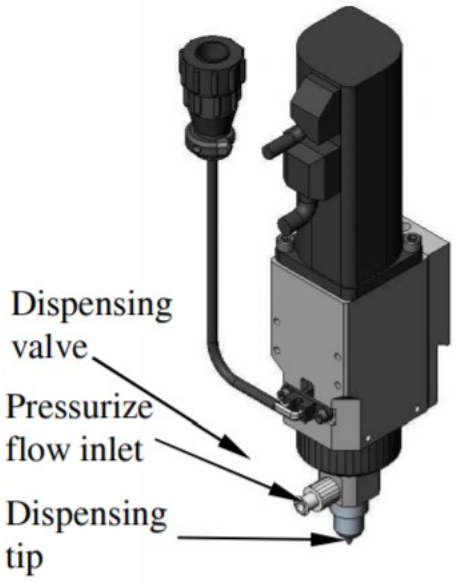

Figure 2.1. nScrypt dispensing pump. Reproduced with permission from [61].

2.3. Infiltration of Printed Inks into Porous Substrate

When an ink drop is deposited on a porous substrate, the interplay of particle motion, solvent evaporation and solvent infiltration into the pores determines the final deposition morphology of the ink drop[62].

The deposition of ink drops onto porous substrates can be divided into three stages as shown in Fig. 2.2: (1) drop impact and spreading; (2) infiltration; and (3) solvent evaporation and particle deposition. A low splashing parameter $K_d = \left[\frac{{d_0}^3 {v_0}^5 \rho^3}{\mu\sigma^2}\right]^{\frac{1}{4}}$ determines the impact of drop on porous substrate, where d_0 is the drop inflight diameter, v_0 is the drop impact velocity, ρ is the density, μ is the dynamic viscosity, and σ is the surface tension of water[63]. Since the substrate pore size is much smaller than the drop size, the spreading process is much faster than the infiltration process. Here the infiltration process is governed by the Washburn[64] equation as shown below:

$$x = \sqrt{\frac{\sigma d_{pore} t cos\theta}{4\mu}} \qquad \text{(E. 1)}$$

Where t is the time for the drop with viscosity of μ and surface tension of σ to penetrate a distance x into the porous substrate with pore size of d_{pore}. We assume that the evaporation process is diffusion-limited and the total evaporation time can be approximated by the Hu-Larson model[65]:

$$t_{EI} = \frac{\pi \rho {d_{depo}}^2 (1 - \frac{V_1}{V_0})}{32D(1-H)c_v} tan\frac{\theta}{2} \qquad \text{(E. 2)}$$

Where D is the diffusivity, H is the relative humidity, c_v is the saturated vapor concentration, d_{depo} is the drop deposition diameter, θ is the apparent contact angle of the drop at the end of spreading process, V_0 is the drop volume and V_1 is the infiltrated volume.

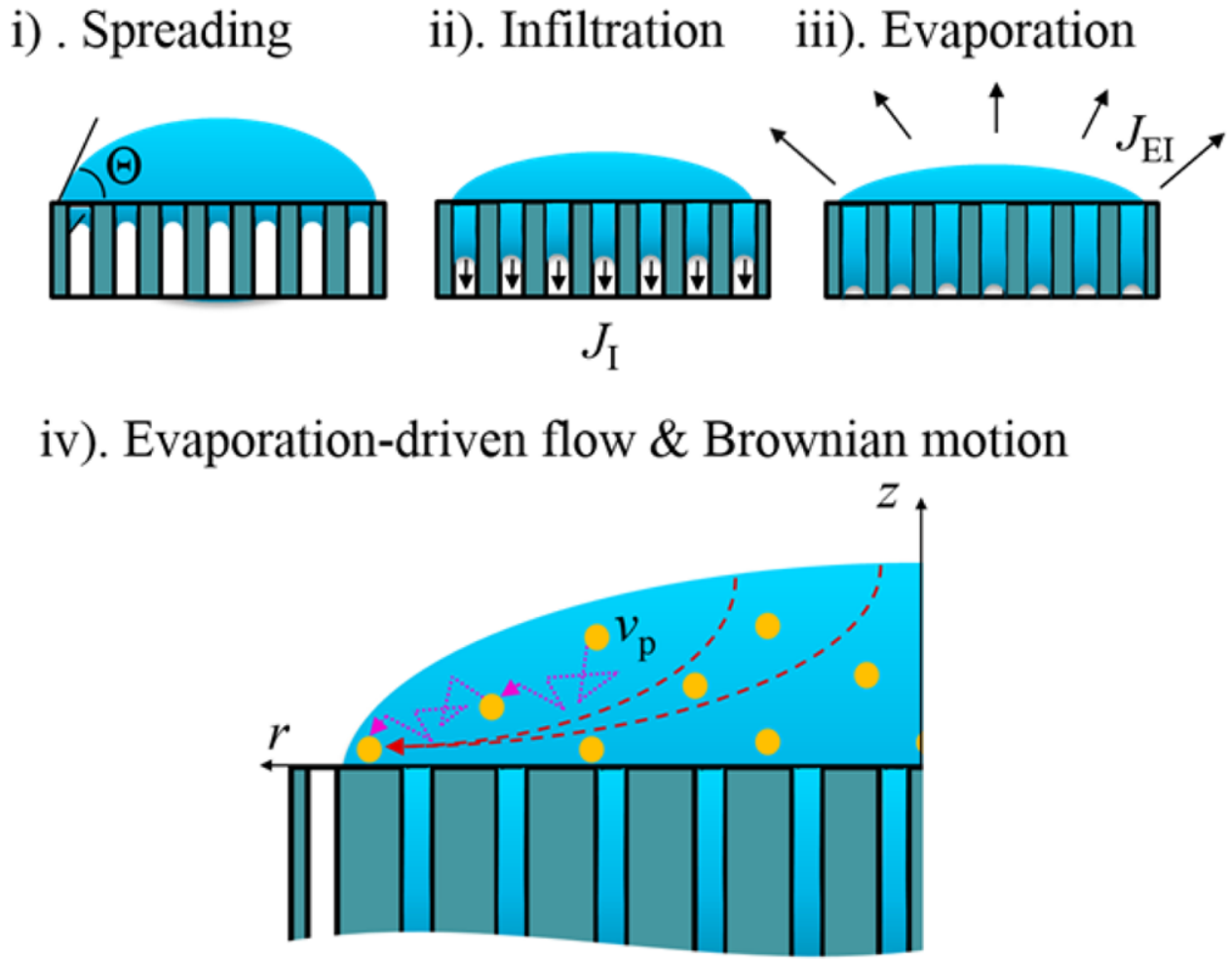

Figure 2.2. 3 stages of drop deposition on a porous substrate: i) spreading process, ii) infiltration process (at flux J_I), and iii) evaporation process (at flux J_{EI}). iv) the interplay of evaporation-driven advection and Brownian motion determines the particle motion in the vicinity of the drop contact line.

The competition between evaporation time of the residual drop left on top of the porous substrate and the particle motion determines whether there is enough time to form a coffee ring before drying out. The ratio of the time to form the first layer of the coffee ring and the evaporation time is given by

$$\frac{t_p}{t_{EI}} = \frac{L_m}{v_p}\frac{2D(1-H)c_v}{V_0^{\frac{2}{3}}\rho}\left(\frac{16}{\pi\tan\left(\frac{\theta}{2}\right)}\right)^{\frac{1}{3}}(1-\frac{V_1}{V_0})^{-1} \qquad \text{(E. 3)}$$

t_p is the time needed for particles to form the first layer of coffee ring; L_m is the distance between two particles in the solution, $L_m=[(V_0-V_1)/N]^{1/3}$ where N is the total number of particles; v_p is the particle velocity determined by both diffusion and advection: $v_p=v_D+v_A$, where v_D is the mean diffusion velocity of the particle approximated by the Einstein diffusion equation[66]: $v_D = \frac{2k_BT}{3\pi d_{part}L_m}$ where k_B is the Boltzmann constant, T is the temperature, and d_{part} is the diameter of the particle. When $t_p/t_{EI}>1$, the evaporation dominates, and it is faster than the time needed for particle to move to the contact line to form the first layer of coffee ring, and as a result, the coffee is suppressed. However, when $t_p/t_{EI}>1$, the coffee ring is formed because particle motion is faster the evaporation.

2.4. Surface Energy Models

Surface Energy Based on Owens-Wendt theory: The surface energy of a solid material is modelled as a summation of the attractive forces with dispersive and polar natures, respectively. The dispersion component was resulted from instantaneous dipoles caused by the motion of electrons within the molecule. The polar component was attributed to the dipole-dipole interactions, such as hydrogen bonding. Therefore, the total surface energy of solid can be yielded as: $\gamma_s = \gamma_s^d + \gamma_s^p$, where γ_s^d is the dispersion component and γ_s^p is the polar component. To determine γ_s, contact angles at the solid-liquid-vapor interface are used as following the Young equation: $\gamma_s = \gamma_{sl} + \gamma_l \cos\theta$, where γ_{sl} is the interfacial energy between the solid and liquid components, γ_l is the surface energy of liquid and θ is the contact angle. According to Owens and Wendt[67], the surface energies can be estimated with the following relationship from modified Young equation,

$$\left(\gamma_s^d \gamma_l^d\right)^{1/2} + \left(\gamma_s^p \gamma_l^p\right)^{1/2} = \frac{1}{2}\gamma_l\left(1+\cos\theta\right), \qquad \text{(E.4)}$$

where γ_l^d and γ_l^p are the dispersion and polar components of the liquid, respectively. All unknowns in the equation (E.4) can be solved by using two-liquid measurement methods.

Interfacial Energy Based on Wu's Model: Here, we estimate the spreading coefficient of the liquid on the solid substrate from the surface energies and their components. At the interface between the liquid and the solid, the equation of state can be obtained following Wu[68, 69] as

$$\gamma_{ls} = \gamma_l + \gamma_s - 4\left[\frac{\gamma_s^d \gamma_l^d}{\gamma_s^d + \gamma_l^d} + \frac{\gamma_s^p \gamma_l^p}{\gamma_s^p + \gamma_l^p}\right] \qquad \text{(E.5)}$$

where, $\gamma_{ls}$is the interfacial surface energy corresponding to the liquid-solid interface, γ_l and γ_s are the surface energies of the liquid and the solid, γ_l^d and γ_l^p are the dispersive and polar components of the liquid, and γ_s^d and γ_s^p are the dispersive and polar components of the solid, respectively. The spreading coefficient is defined as $S = \gamma_s - \gamma_l - \gamma_{ls}$.

2.5. Review of Stretchable Composite Inks Containing Silver Particles

Table 2 compares the conductivities and processing conditions of our stretchable composite ink (see Chapters 4 and 5) with relevant previous works that report stretchable conductive inks that contain silver particles. The field has come a long way, but we addressed some of the important challenges that have been limiting the applications of these inks. Firstly, most stretchable silver inks are screen-printable, not jet-printable, which limits its patterning versatility [70-74]. Secondly, some ink needs multiple-layered printing (5 overlays) to reach high conductivity which increases the complexity of fabrication [74]. Thirdly, some ink needs to be cured at high temperature (more than 100℃), which limits the choice of printing substrate; most commodity fabrics in our everyday life cannot withstand such processing temperatures [70, 71]. Thus, a stretchable and conductive

silver ink that can afford jet printing without requiring additional fabrication steps or high temperature treatments is highly demanded.

Table 2. Comparison study of various silver ink

Components	**Printing method**	**Conductivity value at diff. strain**	**Curing temperature**	**Ref**
Silver-CNT composite, PVDF	Drop casting Hot rolling	5710 S/cm at 0% strain 20 S/cm at 140% strain	160℃, 12 hours	[70]
Ag/Pt embedded rGO mixed with PVDF	Screen printing Hot rolling	3012 S/cm at 0% strain 322.8 S/cm at 35% strain	150℃, 90 min	[71]
Ag trifluoroacetate, SIS rubber, butanone, DMAc(dimethylacetamide)	Printable	1.25 S/cm at 0% strain 0.05 S/cm at 100% strain	Room temperature	[75]
Ag flakes (91 wt%), polyurethane	Screen printing	3570 S/cm at 0% strain 1200 S/cm at 70% strain	70℃, 3 hours	[72]
Ag flakes, MIBK, BCA, fluoroelastomer	Screen printing	0.06 Ω/sq at 0% strain 4.2 Ω/sq at 450% strain	90℃, 2 hours and heat press at 160℃	[74]
Ag flakes, MIBK, fluoroelastomer, fluorine surfactant	Screen printing	4000 S/cm at 0% strain 935 S/cm at 400% strain	80℃, 1 hour and 120℃, 1 hour	[73]
Ag flakes, TEA, MIBK, fluorine rubber	Jet-printing	849 S/cm at 0% strain ~100 S/cm at 110% strain	Room temperature	[76]

Theme 1. Flexible Electronics

Chapter 3. Flexible, Multilayered Printed Circuit Boards and Sensors for Surface Electromyogram

3.1 Introduction

Surface electromyography (sEMG) is a technique for detecting and analyzing electrical signals produced by muscle movements. Recently, there was a rapid advancement in developing wearable health monitoring device systems which can be attached directly onto different parts of body[77]. Such wearable system provides unprecedented opportunities for personal portable devices with remote medicine practices. Multi-functional flexible platform, including real-time sensing, processing, communicating, and integrated power, is central for such wearable health monitoring systems. Here, we developed a printed flexible circuit board (flex-PCB) and skin-mountable sensor that can measure and process sEMG signals. A simple and cost-effective wax-printing technique was used as a lift-off mask to pattern flexible and highly conductive metallic interconnects. The flexible device measured muscle contraction from various parts of human body. The flexible device with reusable adhesives allowed wearability by following the contour of curvilinear skin topology. The device could afford a moderate amount of folding and twisting. Moreover, it can achieve wireless transmission of sEMG signals to personal laptops.

3.2 Experimental Section

3.2.1 Substrate Material and Processing

The substrate is Kapton® film (75μm, American Durafilm). The film possesses a unique combination of desired properties including excellent physical, electrical, and mechanical properties over a wide temperature range. Also, it has excellent chemical resistance which means there are no known organic solvents for it. Therefore, we applied the Kapton® film as the

substrate for our sEMG applications. Prior to printing, the surface of the substrate was treated with oxygen plasma at 1mTorr vacuum condition (PDC-001, Harrick Plasma) for 10 minutes.

3.2.2 Fabrication of Flex-PCBs and Flexible Sensors

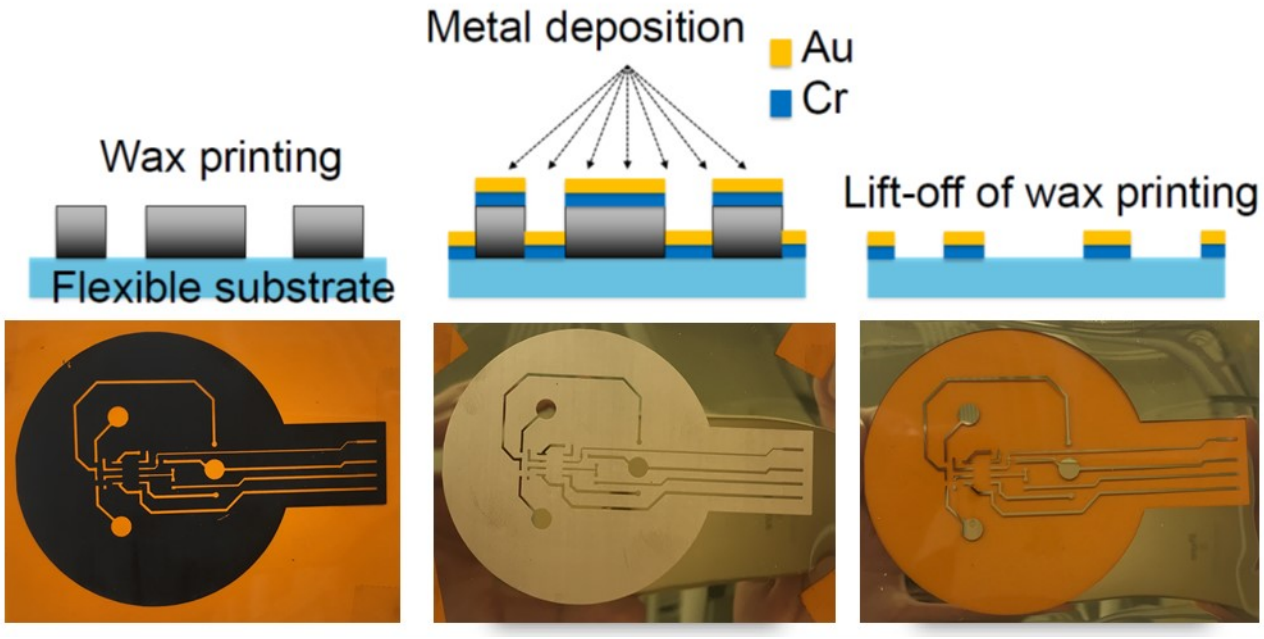

Figure 3.1. Fabrication of Flex-PCBs.

As shown in Fig. 3.1, all drawings of the inverse circuit and electrode patterns (as a sacrificial layer) were done on AutoCAD with micrometer resolution. The patterns were printed onto pre-treated Kapton® film by the wax-printer (Xerox® ColorQube 8570). The wax printer offers excellent print quality and the melting point of the wax is similar to the temperature of boiling water which is ideal for our post-treatment to remove the sacrificial layer[78]. A layer of Cr (20nm) was sputtered (Sputtering System Bob, a planar magnetron sputter system with three sources, vacuum pressure: 10^{-6} Torr, sputtering pressure: 7mTorr, sputtering power: 300W for Cr and 75W for Au) on top of the sample surface and followed by sputtering another layer of Au (50nm). After sputtering, the sacrificial layer and target materials on its surface were washed out

with boiling water. Only the material in the “holes” having direct contact with the substrate stays and forms conductive circuit patterns.

After the removal of sacrificial layers of inverse circuit and electrode patterns, the samples were carefully aligned and attached together by silicone adhesive gel (Silpuran® 2130, provided by Wacker Chemie AG München, Germany). A conductive channel as top-to-bottom interconnect was formed by puncturing the two layers with a 3/8’’ diameter needle, which was dip-coated in the silver paste (EG8050, AI Technology Inc.). Rigid electronics including resistors, conductors, and CPU chips were mounted onto Flex-PCB using the silver paste. After chips mounting, the Flex-PCB was encapsulated with a layer of PDMS (Sylgard 184, weight ratio of curing agent to prepolymer: 1:10) as a protection layer. Another silicone adhesive layer (Silpuran® 2130, provided by Wacker Chemie AG München, Germany) was adhered to the electrode layer to achieve stable adhesion between skin surface and the device.

3.2.3 Electrical and Mechanical Test

Electrical properties of the wax-printing Flex-PCB were measured from a rectangular strip. The rectangular strip was 0.2 mm in width and 40 mm in length. Cyclic reliability on electrical resistivity of the Flex-PCBs with rectangular strip was tested over a 20,000 compress-release cycles.

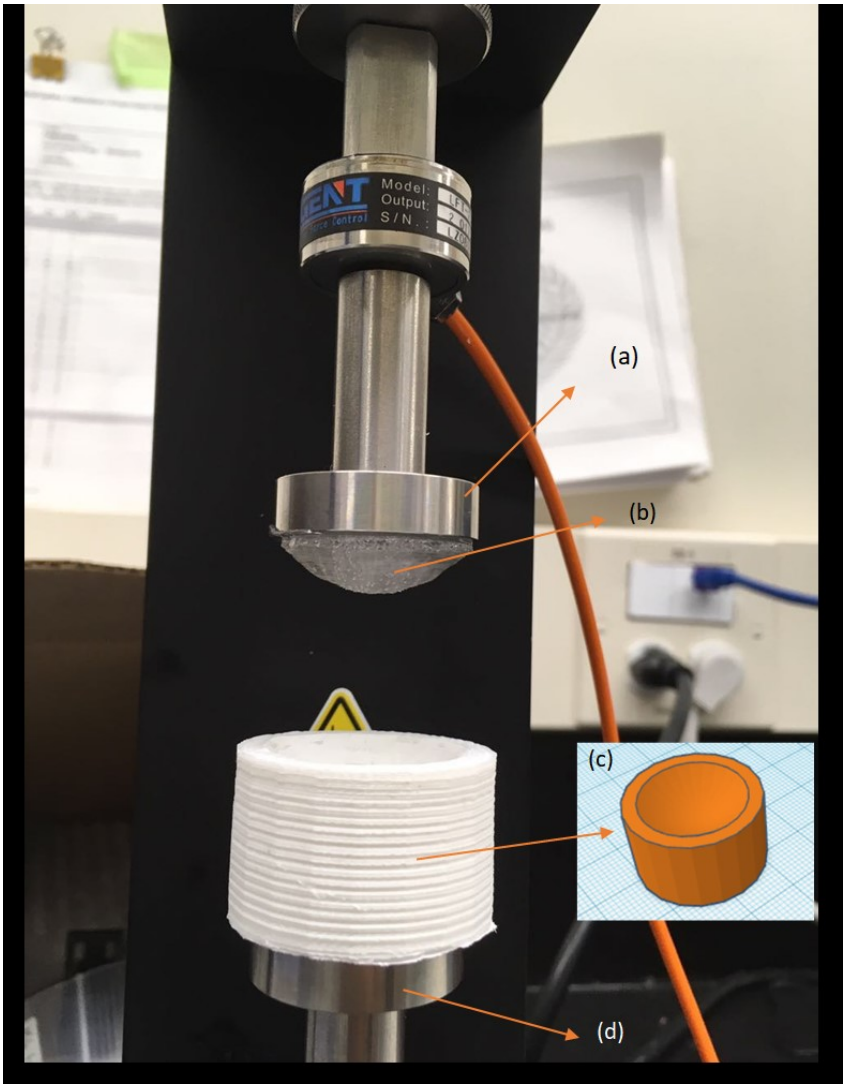

Figure 3.2. Setup for compression test apparatus. (a) load cell, (b) upper part (PDMS model), (c) bottom model, (d) platen.

The compression test setup is shown in Fig. 3.2. The bottom model, a cylinder with a hemisphere hole, was printed by 3D printer (Fig. 3.2 (c), PLA material, parameter of hemisphere hole: radius=15mm). The upper part (Fig. 3.2 (b)) was fabricated by pouring PDMS (Sylgard 184, weight ratio of curing agent to prepolymer: 1:5) into the bottom model and curing at 70℃ for 2 hours. After curing, the PDMS model was took out from the bottom model with a cutter carefully and attached to the load cell (Fig. 3.2 (a)) with a double-sided clear transparent acrylic

elastomer tape (VHB-4910, 3M). Finally, the bottom model was attached on top of the platen (Fig. 3.2 (d)) with VHB tape.

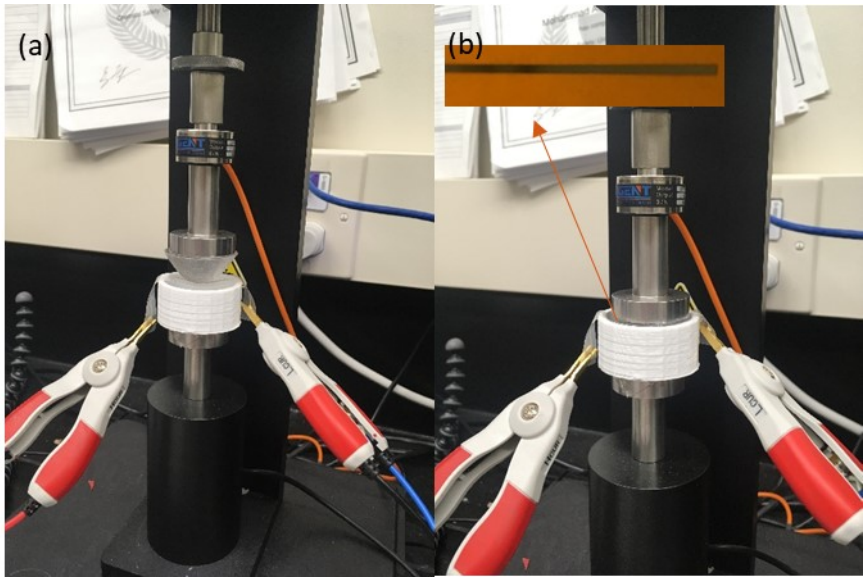

Figure 3.3. Apparatus for compression test. (a) zero point. (b) compression point.

The rectangular strip was attached to the electrical wires and connected to Keithley 2400 SourceMeter. The test piece was put on top of the bottom model and ensured that the strip part is at the center of the model as shown in Fig. 3.3 (a). In the zero position, the test piece was placed on top of the bottom model while touching the PDMS model. The test piece was compressed at a rate of 0.5 Hz by moving the actuator toward to the bottom as shown in Fig. 3.3 (b). The test piece was ensured to return to the zero position after every compression. The mechanical data was collected by CellScale and the electrical data was collected by Keithley 2400 SourceMeter.

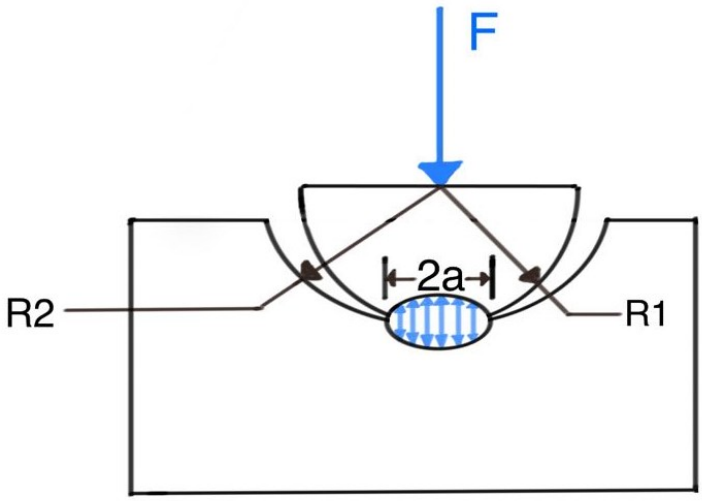

Figure 3.4. Hertz contact stress in the case of a male sphere-female sphere contact.

We applied Hertz contact mechanics[79] to calculate the pressure on the sample. In our case, the model is a sphere-sphere contact as shown in Fig. 3.4. A relative diameter of curvature is defined:

$$\frac{1}{d^*} = \frac{1}{d_1} + \frac{1}{d_2} \qquad \text{(E.6)}$$

Where d_1 is the diameter of the male part (positive) and d_2 is the diameter of the female part (negative).

Effective elastic modulus is defined:

$$\frac{1}{E^*} = \frac{1-{v_1}^2}{E_1} + \frac{1-{v_2}^2}{E_2} \qquad \text{(E.7)}$$

Where v_i and E_i are the Poisson's ratio and Young's modulus of the material i.

The contact area of sphere-sphere model is a disk whose radius is:

$$a = \left(\frac{3F}{8}\frac{d^*}{E^*}\right)^{\frac{1}{3}} \qquad \text{(E.8)}$$

The maximum contact pressure at the center of the circular contact area is given by Hertz as:

$$P_{max} = \frac{3F}{\pi a^2} \qquad \text{(E.9)}$$

In our case, we apply constant force of 100 N. $d_1=d_2=2r=30$ mm. Young' modulus of PDMS (weight ratio of curing agent to prepolymer: 1:5) is 3.6 MPa[80]. Young's modulus of PLA is 3.5 GPa[81]. Poisson's ratio of PDMS is 0.50[82]. Poisson's ratio of PLA is 0.36[83]. Thus,

$$\frac{1}{d^*} = \frac{1}{d_1} + \frac{1}{d_2} = \frac{1}{30mm} + \frac{1}{30mm} = \frac{1}{15mm}$$

$$\frac{1}{E^*} = \frac{1-{v_1}^2}{E_1} + \frac{1-{v_2}^2}{E_2} = \frac{1-0.5^2}{3.6MPa} + \frac{1-0.36^2}{3.5GPa} = 0.208MPa^{-1}$$

$$a = (\frac{3F}{8}\frac{d^*}{E^*})^{\frac{1}{3}} = (\frac{3\times100N}{8} \times 15mm \times 0.208MPa^{-1})^{\frac{1}{3}} = 0.00489m$$

$$P_{max} = \frac{3F}{\pi a^2} = \frac{3 \times 100N}{\pi \times (0.00489m)^2} = 4MPa$$

3.3 Result and Discussion

3.3.1 Wax-printed Conductive Traces

The key advantage of our wax-printing technology is that the combination of Cr and Au offers high conductivity which is 2.5×10^7 S/m as shown in Table 3. The maximum resolution of wax-printing technique is limited by the printer resolution. As shown in Fig. 3.5 (a), the maximum resolution of this technique can reach 0.1 mm.

Table 3. Conductivity and resolution of interconnects on flex-PCBs

Material	Conductivity (S/m)	Resolution (mm)	Flexibility	Reference
Au	2.6×10^7	1.5	Stretchable 50% strain	Drack et al. 2015[84]
Ag	2.9×10^7			
AgNWs	0.2×10^7	0.5	Stretchable 50% strain	Tybrandt & Vörös 2016[85]
Cr/Au	**2.5×10^7**	**0.1**	**Flexible**	**Current work**

3.3.2 Integration of Electrical Components

The silver paste, a highly conductive and sticky material, was used for attaching electrical components onto the flexible substrate. After cured at 120 ℃ for 2 hours, the sticky silver paste became rigid and formed stable connection between the substrate and electrical components. As shown in Fig. 3.5 (b), the integrated flexible device can withstand a certain degree of bending.

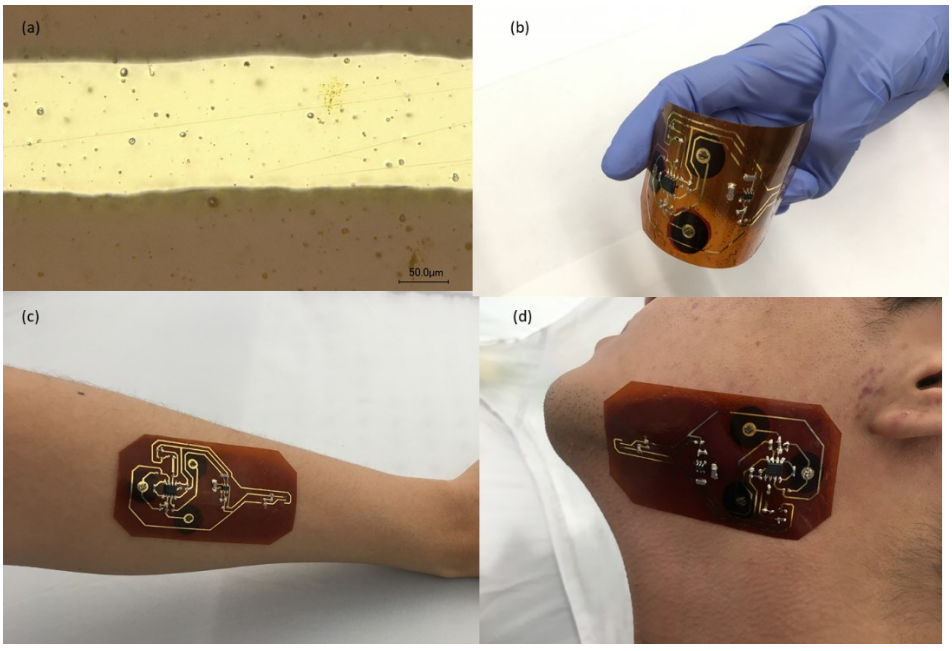

Figure 3.5. (a) Confocal microscope image of wax-printed interconnects. (b) Flexible version of Mobili-T device for sEMG. The flexible device was attached onto forearm (c), and chin (d) of a human subject.

3.3.3 Electrical Properties of Wax-printed Traces

The electrical properties of wax-printed interconnects were measured from a rectangular strip. The rectangular strip was 0.2 mm in width and 40 mm in length. Fig. 3.6 shows the change in resistance under pressure of 4MPa cyclic compression test at a rate of 0.5 Hz. The resistance only increased 1.05 times over 20,000 cycles of compression test which demonstrated excellent electrical and mechanical stability of the wax-printed traces.

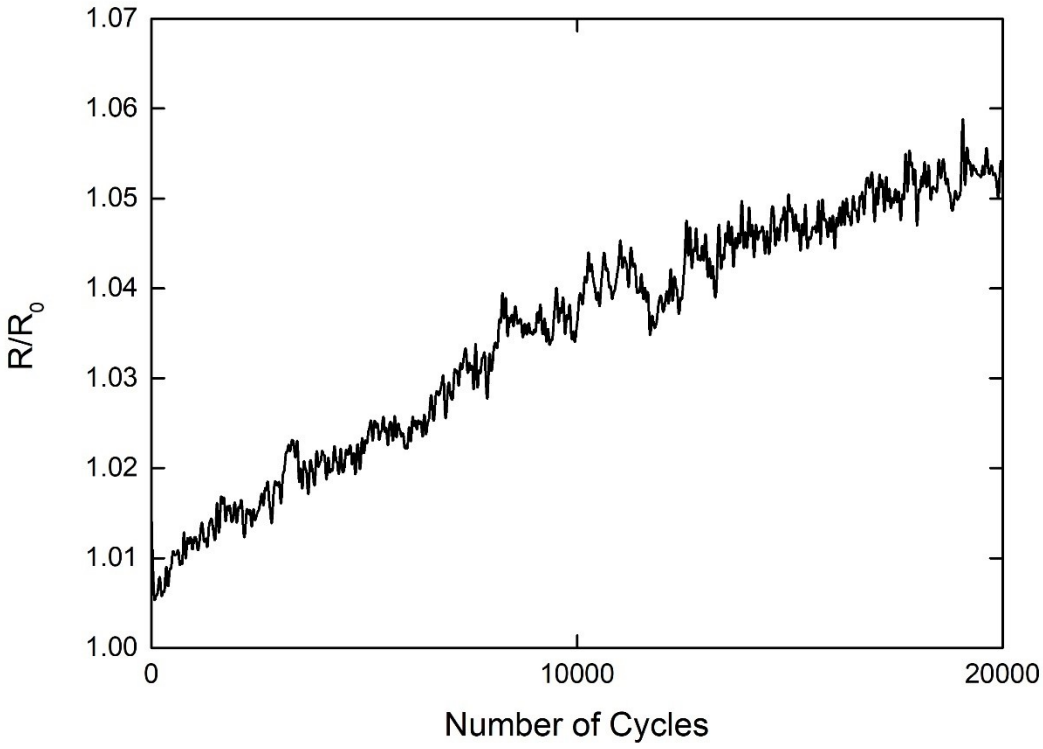

Figure 3.6. Resistance change versus number of compression (4 MPa) cycles for wax-printed interconnects.

3.3.4 Multi-layered Printed Circuit Boards for sEMG

The multi-layered printed circuit board was achieved by aligning and attaching circuit substrate and electrode substrate together with adhesive silicone gel. The two-layered design

allowed precise targeting of the sensory area on human skin without crosstalk. The conductive channel between two layers was formed by simply injecting a small of the silver paste by a needle to allow electrical connection between electrodes and circuit across the whole substrate thickness. Another layer of adhesive silicone gel was applied to the electrode layer to achieve reusable and stable connection.

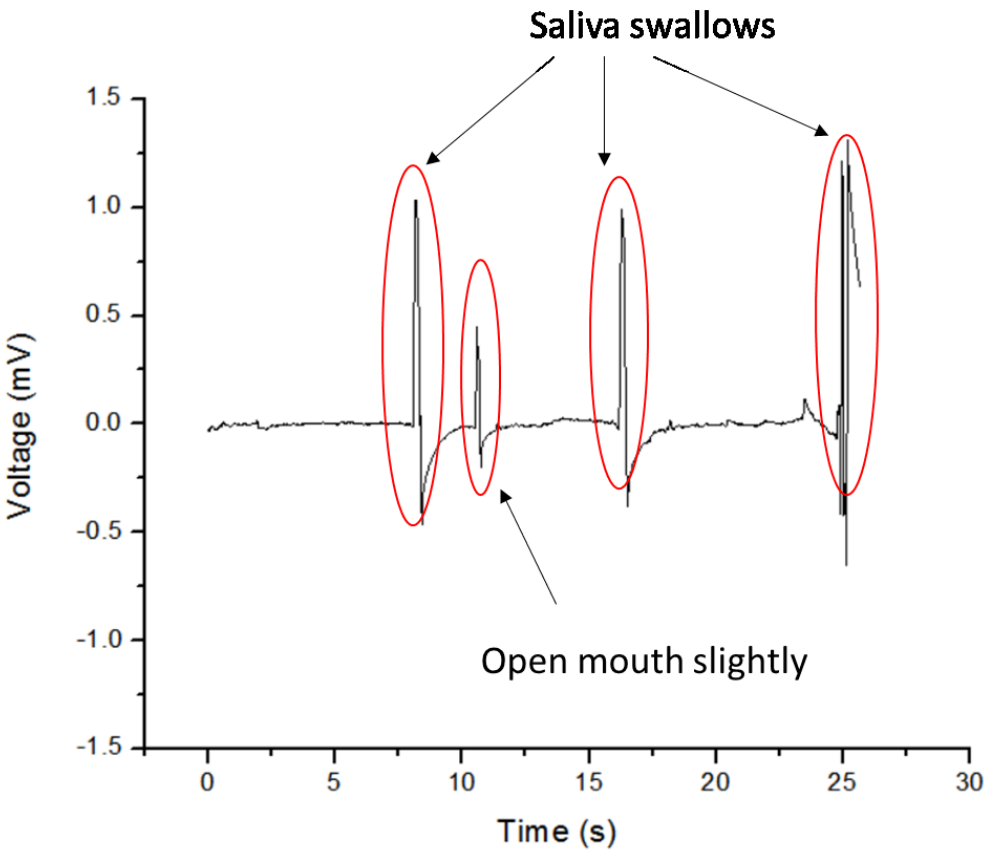

Figure 3.7. Signal collected by sEMG patch for saliva swallows.

The multi-layered flexible device with all electrical components was connected to a battery (soldered with wires). The Bluetooth wireless chip transmitted sEMG signals to data receiving electronics. The sEMG system is fully integrated, portable and compact. The signal

contamination was successfully eliminated because of the two-layered design allowing separation of the circuit and electrodes on two substrates. As a demonstration, the sEMG system was worn on the submental space to detect the saliva swallows. The reference electrode was placed on the mandible while the other two electrodes were over the suprahyoid muscles separately during saliva swallowing and mouth opening/closing. The participant was asked to look straight ahead and swallow their saliva (3 trials). The sEMG signals were successfully collected as shown in Fig. 3.7.

3.4 Conclusion

In this work, we developed a versatile technology with capability of rapid, simple, customizable fabrication of flexible printed circuit boards and sensor. The printed interconnects had a conductivity of 2.5×10^7 S/m and could afford a moderate amount of folding and twisting. The reliability tests of the interconnects showed that there was almost no change of electrical properties over 20,000 cycles of compressing test at pressure of 4 MPa. The resolution of the interconnects was controlled by the design of the wax-printer which reached 100μm. Multi-layered device was achieved with a one-step simple fabrication. Finally, the flexible system for sEMG sensing was designed, fabricated, and fully electrical integrated. With the help of reusable silicone adhesive, the flexible device allowed wearability by seamlessly following the contour of curvilinear skin topology.

Theme 2. Stretchable e-Textiles

Chapter 4. Two-layered and Stretchable e-Textile Patches for Wearable Healthcare Electronics

4.1 Introduction

Stretchable electronics with physiological sensing abilities, such as electrical signals,[86] electrochemical signals from sweat,[87, 88] temperature,[84, 89] tactile force,[90] and blood glucose,[91] have been a new leading trend in wearable healthcare. While the technology promises an intimate and comfortable integration to the human body, employing e-textiles may be the most efficient path forward. The necessary first step towards healthcare application of e-textile is on the sensory patches that are in direct contact with human skin.[92, 93] For meaningful healthcare applications, such e-textile sensory patches connect with electrical circuits that enable signal transduction and wireless communication abilities.[94, 95]

In this work, we develop a stretchable, yet mechanically and electrically robust e-textile sensory patch along with an electronic system for wearable healthcare applications. Here, silver-based fluoroelastomer composite ink forms conducting traces via jet printing, where the ink's penetration depth into electrospun porous polyurethane textile is controlled by utilizing the size and shape of silver particles, thus to enable two-layer configuration (Figure 4.2). Compared to the conventional single-layer structure for sensory patches, the two-layer structure enables a simple and reliable definition of electrode areas while the conducting traces are intrinsically separated from human skin. The traces in the e-textile show a high conductivity of ≈3000 S/cm with high stretchability and durability over repeated strain cycles. Such high conductivity and durability are achieved by a one-step printing process which does not require any post-treatment. Finally, we demonstrate the

biomedical application of our e-textile-based systems for surface electromyography (sEMG) sensing of human muscles activities in a rehabilitation medicine setting.

4.2 Experimental Section

4.2.1 Nanocomposite Ink Preparation

Fluoroelastomer (DAI-EL G801, Daikin Industries) and methyl ethyl ketone (butanone; M209-1, Sigma Aldrich) were mixed at the weight ratio of 1:2.55 with a magnetic stirrer for 6 hours. After the mixing, two types of silver particles, namely Ag-flake (Sigma Aldrich; nominal average flake size of 10 μm) and Ag-powder (Sigma Aldrich; nominal average particle size of 2 – 3.5 μm) were added into the respective solution at the ratio of 3:1 (weight ratio between silver particle and electromeric fluoropolymer), followed by mixing with magnetic stirrer for 4 hours. Subsequent bath sonication for 10 minutes ensured a well-dispersed ink for printing. All procedures are carried out at the room temperature.

4.2.2 Substrate Material and Processing

The textile substrate is NANOSAN®-Sorb (Nanofiber Technology, LLC), a nonwoven textile of thermoplastic polyurethane nanofibers. The textile has a moderate absorbency from 2.5 to 18.5 g/g (i.e. absorbed liquid/textile in mass) when soaked in saline solution (0.9% NaCl in water) for 30 minutes, according to NWSP 240.0.R2 (15) standard test. In addition, its flexibility, elasticity, resilience, and ductility make the textile suitable for biomedical applications as sweat and blood absorbent. Therefore, we employed the textile as the substrate for our sEMG applications. Prior to printing, inner and outer surfaces of the porous substrate were treated with oxygen plasma at 1 mTorr vacuum condition (PDC-001, Harrick Plasma) for 10 minutes.

4.2.3 Printing of Nanocomposite Ink

The prepared ink was loaded to a custom-designed syringe (Tabletop-3Dn, nScrypt; Figure 4.1). A sheet of the PU nanotextile (NANOSAN®-Sorb) was cut into a rectangular shape of 120 mm × 120 mm and pre-treated in oxygen plasma for 10mins. The nanotextile sheet was placed in the printer bed which was kept at room temperature during printing. For each printing, 10 mL of the prepared ink was loaded to a syringe. After the printing, air drying at room temperature was sufficient for all applications. The samples used for analysis were dried in vacuum chamber at room temperature for 8 hours for complete removal of the solvent.

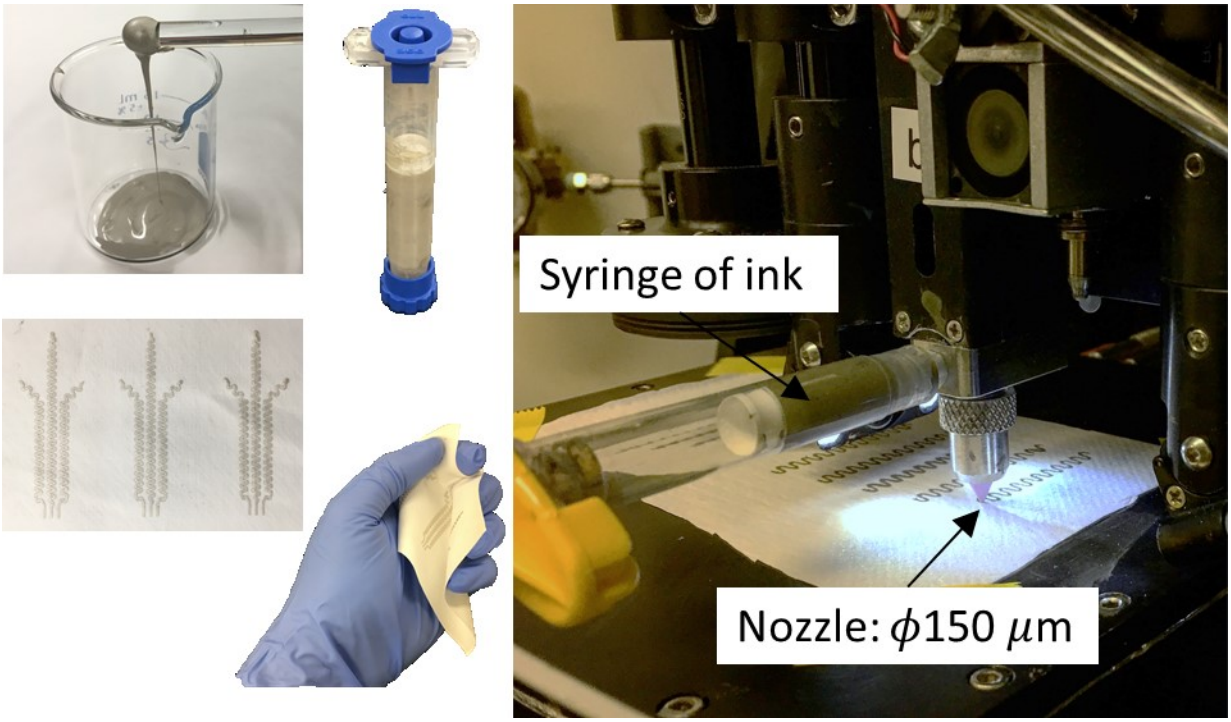

Figure 4.1. Printing of the composite ink

4.2.4 Two-layered E-Textile Patches[1]

[1] The idea for section 3.2.4 is from Dr. Thanh-Giang La.

After printing one side, the samples were flipped to the other side and loaded to the printer. The samples were carefully aligned with the aid of laser marking. After printing patterns on both sides, vertical interconnect access (VIA) was formed by puncturing the e-textile using a 3/8" diameter needle, which was dip-coated in the prepared ink.

4.2.5 Surface Energy Measurement

In this work, the surface energies of the two types of dried Ag/fluoro-elastomer inks and compressed electrospun polyurethane textile substrate were estimated by measuring contact angles.

In order to prepare the solid surface of dried composite ink, the composites inks were brushed onto glass slides, then dried in vacuum at 20 ºC to form ~200 μm-thick films.

In order to prepare the solid surface of the polyurethane textile substrate for contact angle measurement, the porous substrate must be compressed and flattened. Here, three 2 cm x 2 cm sheets of the polyurethane-based textile (3 [sheets] × 300 [μm thick / sheet]) were stacked between two polyimide (PI) films (Kapton, 50 μm thick). The PI/textile/PI stack was loaded on to a holder of a hydraulic hot-pressing machine (Carver, Inc.). The textile was compressed at a pressure of 500 kPa and heated at 80 ºC for 2 hours, which resulted in a 400 μm-thick smooth film. The film was treated with oxygen plasma just prior to the contact angle measurement to mimic the actual condition for the printing process.

4.2.6 Electrical and Mechanical Test

Mechanical and electrical properties of the trace-printed e-textiles were measured from a rectangular strip and a serpentine trace printed with Ag powder composite inks. The rectangular

strip was 4 mm in width and 40 mm in length. The serpentine traces had 0.5 mm linewidth, 2 mm lateral amplitude, 40 mm length, and 2 mm pitch interval.

Uniaxial stress–strain curves of the pristine textile and the two types of printed e-textiles were measured over 5 stretch-release cycles up to 50% strain. Cyclic reliability on electrical resistivity of the e-textiles with serpentine traces was tested over a thousand stretch-release cycles. Here, three maximum strains, up to 10%, 20%, and 30%, respectively, were applied with a stretch/release strain rate of 4% per second.

4.3 Results and Discussion

4.3.1 Printing Conductive Traces

The key advantage of our printing technology is that it is one-step processing without post-treatment as shown in Figure 4.2 (a). In contrast, available commercial silver ink requires thermal annealing at temperatures higher than 130°C[96]. We printed a nanocomposite ink on a nonwoven thermoplastic polyurethane (PU) substrate (SNS Nanosan®-Sorb[97]), in which the electrospun fibrous structure provides stretchability. The substrate is developed for human skin contact applications, thus is breathable for air permeation and slightly hydrophilic to absorb a moderate amount of sweat and contaminants. A scanning electron microscope (SEM) image of the textile substrate in Figure 4.2 (b) shows fibrillar structure with highly polydisperse diameters ranging from 100 nm to 10 μm, which also provide an open porous structure for conductive ink infusion. The 300 microns thick textile is reported to have a stretchability up to 120% when uniaxially strained, whereas full dimensional recovery is available below 50% of strain. The soft and conformal nature of the e-textile is preserved after the printing process in Figure 4.2 (c).

The composite ink was prepared by mixing conductive silver particles (Sigma Aldrich, and two species of the conductive particles were used as silver flakes with average particle size of 10 μm,[98] and silver powders with average particle size of 2-3.5 μm[99]) and fluoro-elastomer (DAI-EL® G-801, DAIKIN) in methyl ethyl ketone (butanone) (Figure 4.2 (d)). The prepared viscous ink was loaded to a jet-printer (Tabletop-3Dn, nScrypt). Ink droplets were expelled via a 150-micron nozzle at a pressure of 10 kPa relative to atmospheric pressure (controlled by the software associated with the printer) onto the textile substrate, which was oxygen plasma treated right before the printing process. Upon deposition, the textile substrate absorbed a certain amount of the ink microdroplets into its porous internal structure. When the solvent in the microdroplet dried in a fume hood at 22 ºC for 8 hours, an 80 micron-thick skin-layer of dried ink is formed on the surface of the textile substrate. At the same time, there formed a 30 micron-deep cladded-layer, wherein the conductive ink form cladding along the nanofibers in the inner part of the textile substrate (Figures 4.2 (e)-(h)). Such cladded-layer benefit the mechanical durability, conductivity, and adhesion of conductors to the textiles. These advantages play the key roles in performance of e-textiles when integrated to a full electronic system.

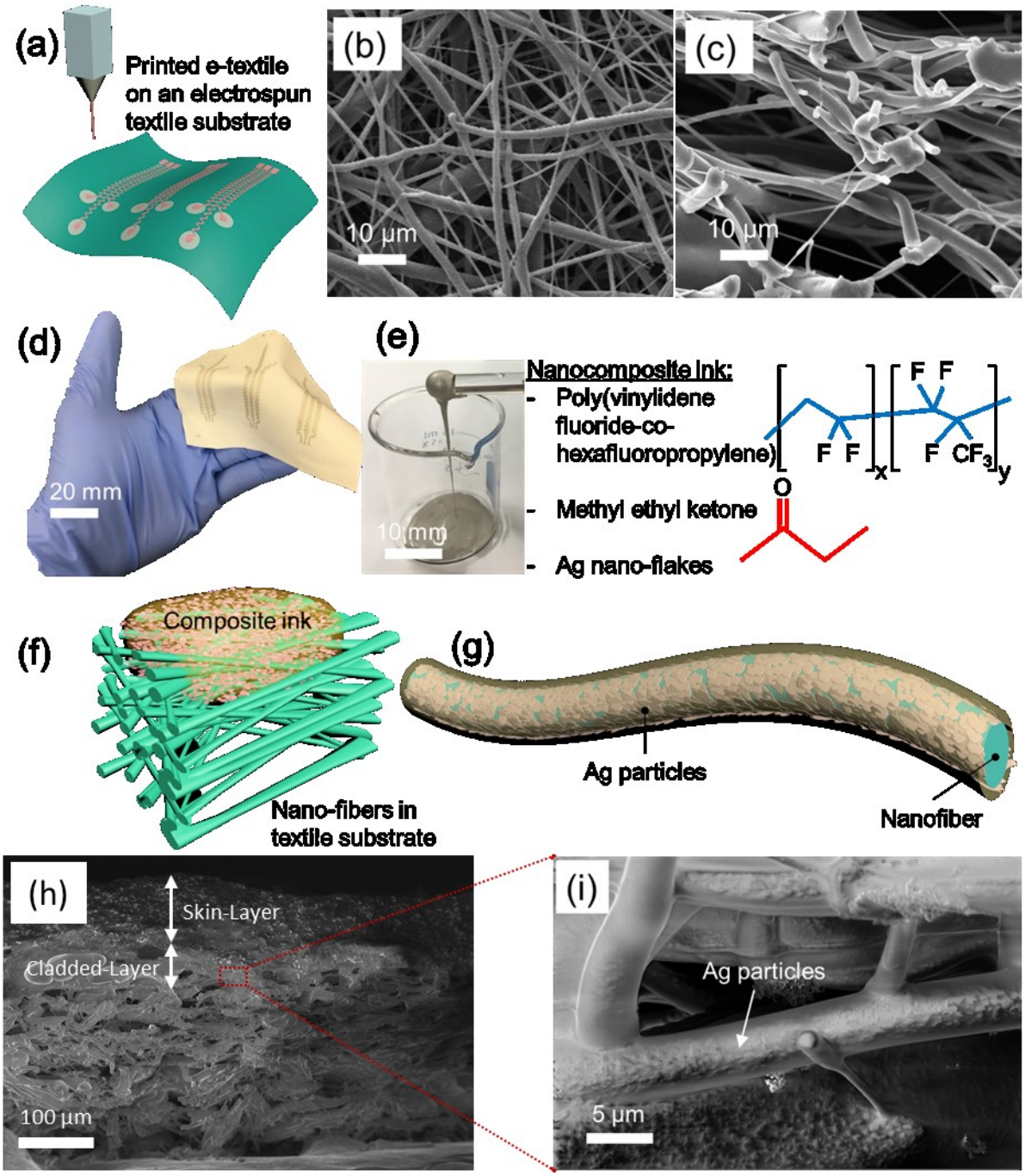

Figure 4.2. Printed, stretchable e-textile conductors. (a) The conceptual drawing of jet-printing nanocomposite inks onto a textile substrate. Scanning electron microscope (SEM) image of the textile substrate, which was compressed electrospun nanofibers of polyurethane: (b) top view and (c) cross-section view. (d) A sheet of e-textile with printed conductive serpentine traces. (e) Prepared nanocomposite ink which consists of silver particles, fluoroelastomer, and methyl ethyl ketone. (f) A schematic illustration of printed ink on the textile substrate. (g) A schematic illustration of a single cladded nanofiber in the cladded-layer of printed e-textile. SEM images of (h) cross sectional view of the e-textile after ink printing, and (i) the close-up view of the cladded-layer.

4.3.2 Effects of Ag Particles on Permeation of Composite Ink into Nanotextiles

In this work, we used two species of Ag particles with different shape and average particle sizes, such as (i) flakes with the *average size* of 10 μm metal traces (denoted as Ag flakes hereafter), and (ii) powders with *average size* of 2 – 3.5 μm metal traces (denoted as Ag powders). The '*average size*' values are stated as we received from the vendor (Sigma Aldrich), however the actual size distribution of individual particles (flakes or powders) were extremely polydisperse in nature. Especially, the existence of nanosized particles seem to affect the properties of e-textiles. The SEM image of the Ag flakes reveal that each particle is predominantly larger than micrometers in size with irregular shapes (Figure 4.3 (a)), whereas many particles in the Ag powders had sizes around (or even less than) 200 nm (Figure 4.3 (b)). These small particles efficiently permeate into the pores of the textile substrate, resulting in the formation of cladded-layer shown in Figures 4.3(f) and (h). Figures 4.3 (c) and (d) show the cross section of the *printed inks* (i.e., Ag particles *with fluoropolymers* after solvents were dried). The printed ink containing Ag flakes showed distinctively smaller permeation depth into textile structure (Figure 4.3 (c)) when compared to the printed ink with Ag powders (Figure 4.3 (d)).

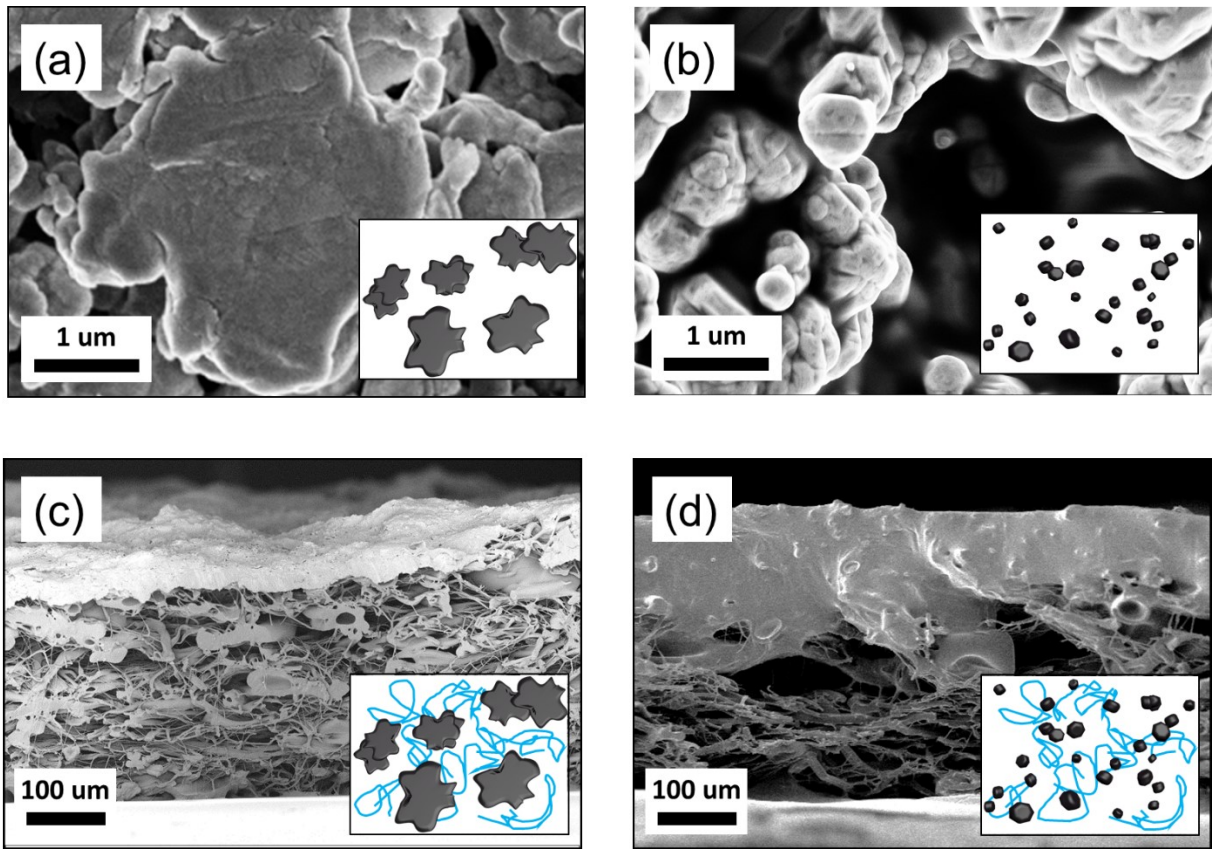

Figure 4.3. SEM images of (a) Ag flakes (b) Ag powders. Ag powders contain finer Ag particles than Ag flakes, as illustrated in the cartoons in the insets in (a) and (b). Cross sectional SEM images printed e-textiles with (c) Ag-flake-based and (d) Ag-powder-based composite inks. The insets in (c) and (d) depict the existence of fluoropolymers in the composite inks (drawn not to scale).

4.3.3 Electrical and Mechanical Properties of the Printed e-Textile

Mechanical and electrical properties of the trace-printed e-textiles were measured from a rectangular strip (Figure 4.4 (a)) and a serpentine trace (Figure 4.4 (b)) printed with Ag powder composite inks. The rectangular strip was 4 mm in width and 40 mm in length. The serpentine traces had 0.5 mm linewidth, 2 mm lateral amplitude, 40 mm length, and 2 mm pitch interval. After drying, the original values of resistance are 0.22Ω for the rectangular strip and 4.1Ω for the serpentine trace. Figure 4.4 (c) shows the change in resistance ratio (as, the ratio of the resistance

under strained over the original value) under uniaxial strains from zero to 125% The resistance of the e-textile sample with the rectangular strip increased 412-fold at 60% strain, whereas the increase was only 24.7 times of the original value at even higher strain of 120% in the serpentine sample.

Uniaxial stress–strain curves of the pristine textile and the two types of printed e-textiles were measured over 5 stretch-release cycles up to 50% strain (Figure 4.4 (d)). As expected for viscoelastic materials, hystereses were observed in all measurements to different degrees. However, all samples showed full recovery (i.e. closed-loop cycles that ends at zero strain when stress reduces to zero) at the end of each cycle. Figure 4.4 (e) shows cyclic mechanical reliability on electrical resistivity of the e-textiles with serpentine traces over a thousand stretch-release cycles. Here, three maximum strains, up to 10%, 20%, and 30%, respectively, were applied with a stretch/release strain rate of 4% per second. Although the resistance values gradually increased with increasing cycles, the relative increase in resistance values were within the same order of magnitude even after one thousand cycles even at 30% maximum strain.

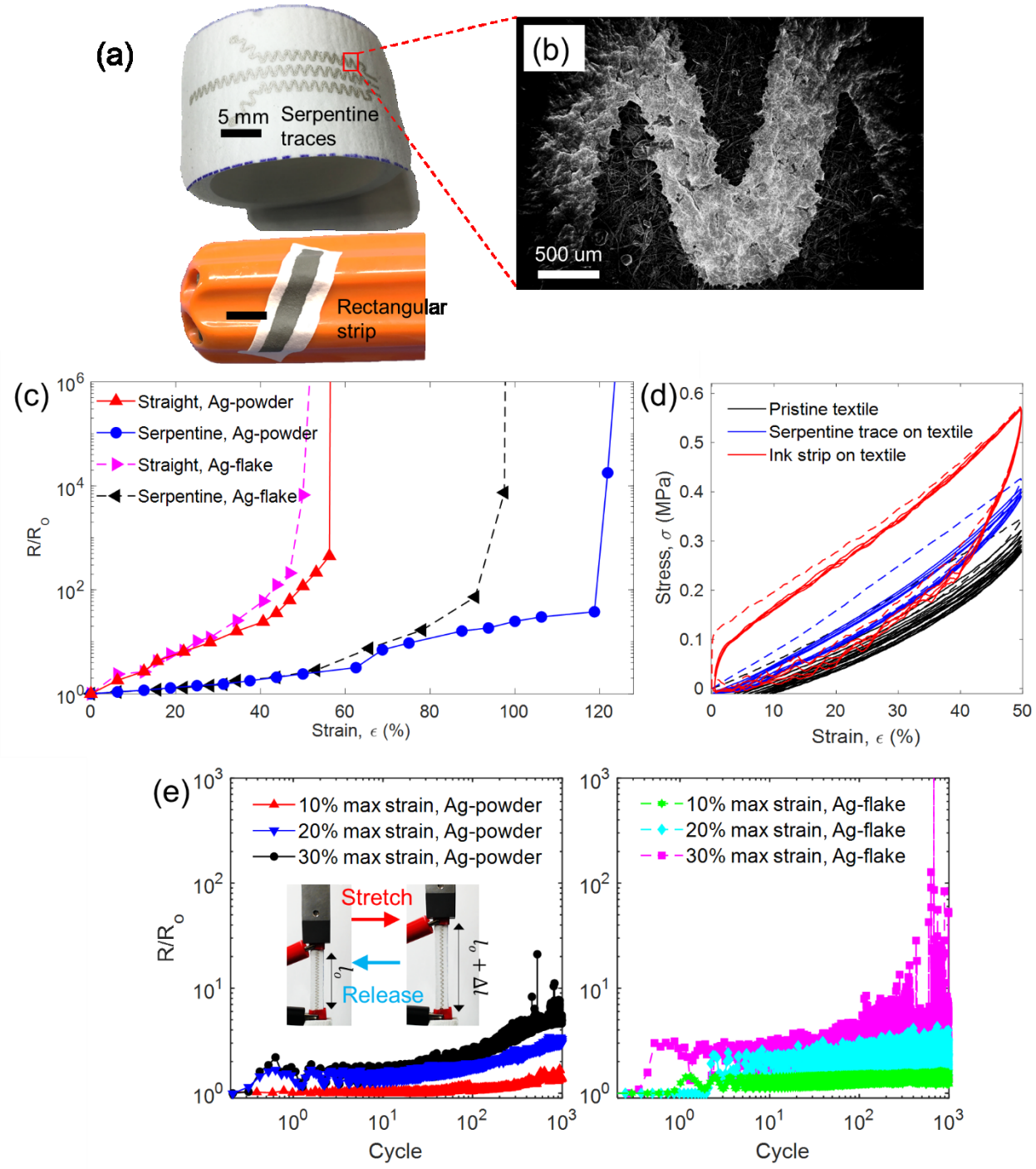

Figure 4.4. (a) Stretchable printed e-textiles with a serpentine (up) and a straight (rectangular) shaped traces. (b) SEM image of the serpentine trace. (c) Changes in resistance of the serpentine and straight traces under uniaxial tensile stress conditions. (d) Cyclic stress-strain curves (5 cycles; dashed lines denote the first loop) for the pristine textile and printed e-textiles. Reliability tests from serpentine-printed e-textile

samples wherein the composite inks contain (e) Ag-powder and (f) Ag-flake, respectively.

4.3.4 Surface Energy

In our experiment, a stable coating of the nanocomposite ink on the textile substrate is helpful for operational reliability of the e-textile. Evaluating surface energies of the inks and the textile by contact angle measurement shed light on understanding the coating stability between the two materials. Here, we use deionized water (polar) and 1-bromonaphthalene (nonpolar) as the two testing liquids, whose dispersion and polar components were given as in Table 4. ~200 micron-thick layers of the two conducting nanocomposite inks were deposited on different glass slides and then thoroughly dried. Subsequently, deionized water and 1-bromonaphthelene droplets as testing liquids were applied on the dried inks, while the contact angles were digitally measured by a goniometer (FTA-200, First Ten Anstroms Inc.), as illustrated in Figure 4.5. The dispersion and polar components of the surface energy of the dried inks were estimated according to the Owens-Wendt model.[67] As shown in Table 4, the total surface energy of our dried Ag-powder/fluoroelastomer ink was estimated to be 39.98 mJ/m^2, with the dispersion and the polar components contributing 39.86 and 0.12 mJ/m^2, respectively. For the dried Ag-flake/fluoroelastomer ink, these values were 32.12 mJ/m^2 (total), with 29.89 (dispersion) and 2.23 (polar) mJ/m^2, respectively. To measure solid-liquid contact angles between the textile and the testing liquids, the textile was prepared as a thin film by hot pressing. The total surface energy of the textile was calculated to be 46.68 mJ/m^2 in which the dispersion and polar components were 35.30 and 11.38 mJ/m^2, respectively.

Table 4. Surface energies of the materials

Material	Contact angle (W)	Contact angle (B)	Total SFE (mJ/m^2)	Dispersive component (mJ/m^2)	Polar component (mJ/m^2)
Deionized water (W)	-	-	72.8[67]	21.8[67]	51[67]
1-bromonaphthalene (B)	-	-	43.8[100]	43.6[100]	0.2[100]
Dried Ag powders/ fluoroelastomer ink	105.06±2.87˚	26.33±1.32˚	**39.98**	**39.86**	**0.12**
Dried Ag flakes/ fluoroelastomer ink	126.32±3.24˚	51.85±2.47˚	**32.12**	**29.89**	**2.23**
Polyurethane textile (thin film)	64.91±1.75˚	30.66±1.58˚	**46.68**	**35.30**	**11.38**

***** *SFE: surface energy*

Table 5. Interfacial surface energies and spreading coefficient of the materials

Material	Estimated interfacial surface energy* (mJ/m^2)	Spreading coefficient (mJ/m^2)
Dried Ag powders/fluoroelastomer ink – Polyurethane textile	11.29	-4.60
Dried Ag flakes/fluoroelastomer ink – Polyurethane textile	6.59	7.97

***** *Estimated from equation (E.5)*

Table 5 shows the interfacial energies of the dried Ag-powder-based ink/textile interface and the dried Ag-flake-based ink/textile interface as 11.29 mJ/m^2 and 6.59 mJ/m^2, respectively. The spreading coefficients are estimated to be -4.59 and 7.97 for the Ag-powder-based ink/textile interface and the dried Ag-flake-based ink/textile interface, respectively. Theoretically, it can be interpreted as that the dried Ag-powder-based ink partially spreads on the textile, while the dried Ag-flake-based ink completely spreads on the textile. However, the slightly negative number of the former imply that the existence of the dried Ag-powder-based ink will not be strongly opposed by thermodynamics (*i.e.*, no severe tendency to dewet).

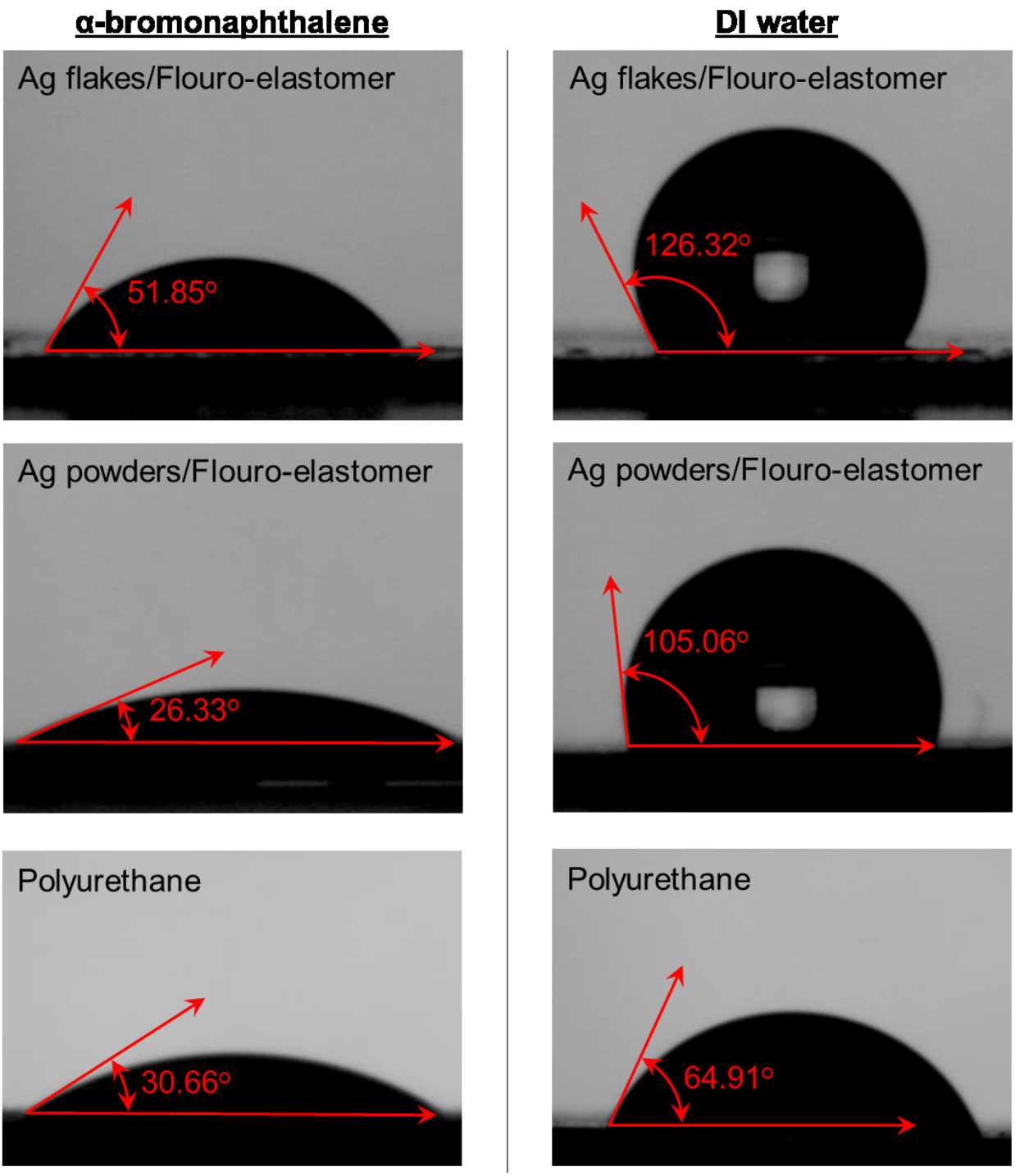

Figure 4.5. Contact angles measurements of model polar (water) and non-polar (α-bromonaphtalene) liquids on solid substrates made of the two types of *dried* inks (Ag flake- and Ag-powder-based, respectively) and pressed polyurethane. Note that the polyurethane substrate is 'pressed' to remove the pores and to smoothen the surface.

4.3.5 Two-layered e-Textile Patches[2]

When the cladded-layer thickness (*i.e.*, ink permeation depth) is controlled to be around a quarter of the textile thickness, as shown in Figure 4.2 (h), electrical insulation between the two sides of e-textile can be assured whereas the cladded-layer helps in achieving better conduction under high strains, as shown in Figure 4.4 (c). Using the design concept, we fabricated a two-layered e-textile patch solely by ink printing, as shown in Figures 4.6 (a) and 4.6 (b). Here, the sensory electrodes were printed on one side and the serpentine traces printed on the opposite side of the textile substrate. The separation of the electrodes and the traces allows precise targeting of the sensory area on human skin, as well as robust electrical insulation required for traces. In addition, an elastomer thin-film (e.g. 200-μm-thick PDMS Sylgard 184, or 250-μm-thick 3M™ VHB double side tape) was used to protectively encapsulate the serpentine traces and hinder detachment of Ag particles. The encapsulating thin-film was patterned by a scan-and-cut machine (Brother CM550DX) to fit the trace layouts. The VIA (Vertical Interconnect Access) between the two layers was formed simply by injecting a small amount of the ink by a needle (0.3 mm diameter) to allow complete permeation across the whole substrate thickness, as shown in the SEM images in Fig. 4.6 (c) and (d). Fig. 4.6 (e) and (f) show that the two-layered e-textile patches can withstand harsh stretching conditions. When applying on human skins, a medical grade double side tape (3M™ 1509 Medical Tape, thickness of 0.12 mm) with relief patterns

[2] The idea for Section 3.3.5 is from Dr. Thanh-Giang La.

was used to achieve conformal attachment while maintaining air/moisture breathability (Fig. 4.7).

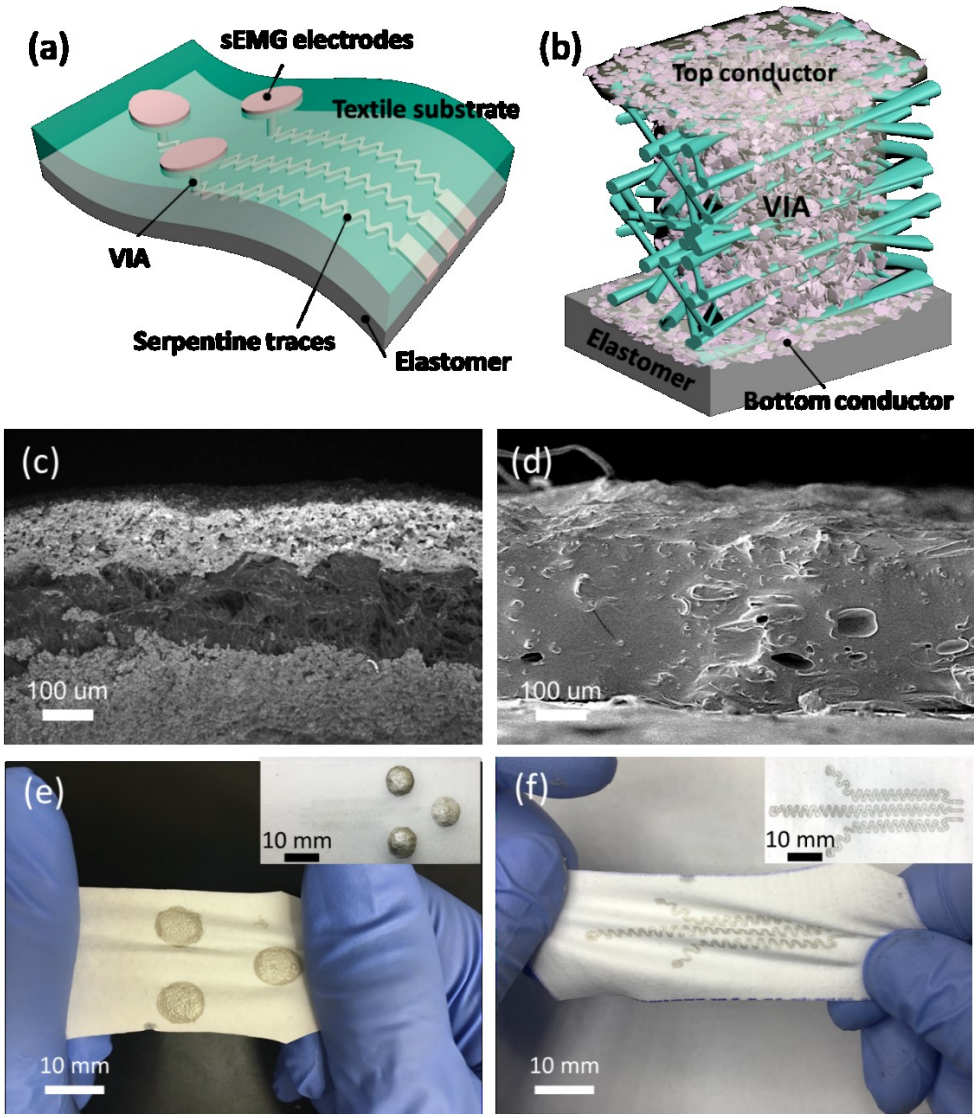

Figure 4.6. Two-layered printed e-textile patches. (a) Schematic of the e-textile patch comprising three printed electrodes, VIAs, and serpentine traces encapsulated by dielectric elastomer (PDMS, or acrylics). (b) An illustration of the VIA. Cross-sectional SEM images of printed two-layered e-textile where each of the layers are electrically (c) insulated by the gap between cladded-layers and (d) conducting through the dried-ink-filled VIA between the printed layers. Top view photographs of the two-layered e-textile seen from (e) the sensory electrode and (f) the serpentine traces sides. The main panels and the insets show stretched and non-stretched states, respectively.

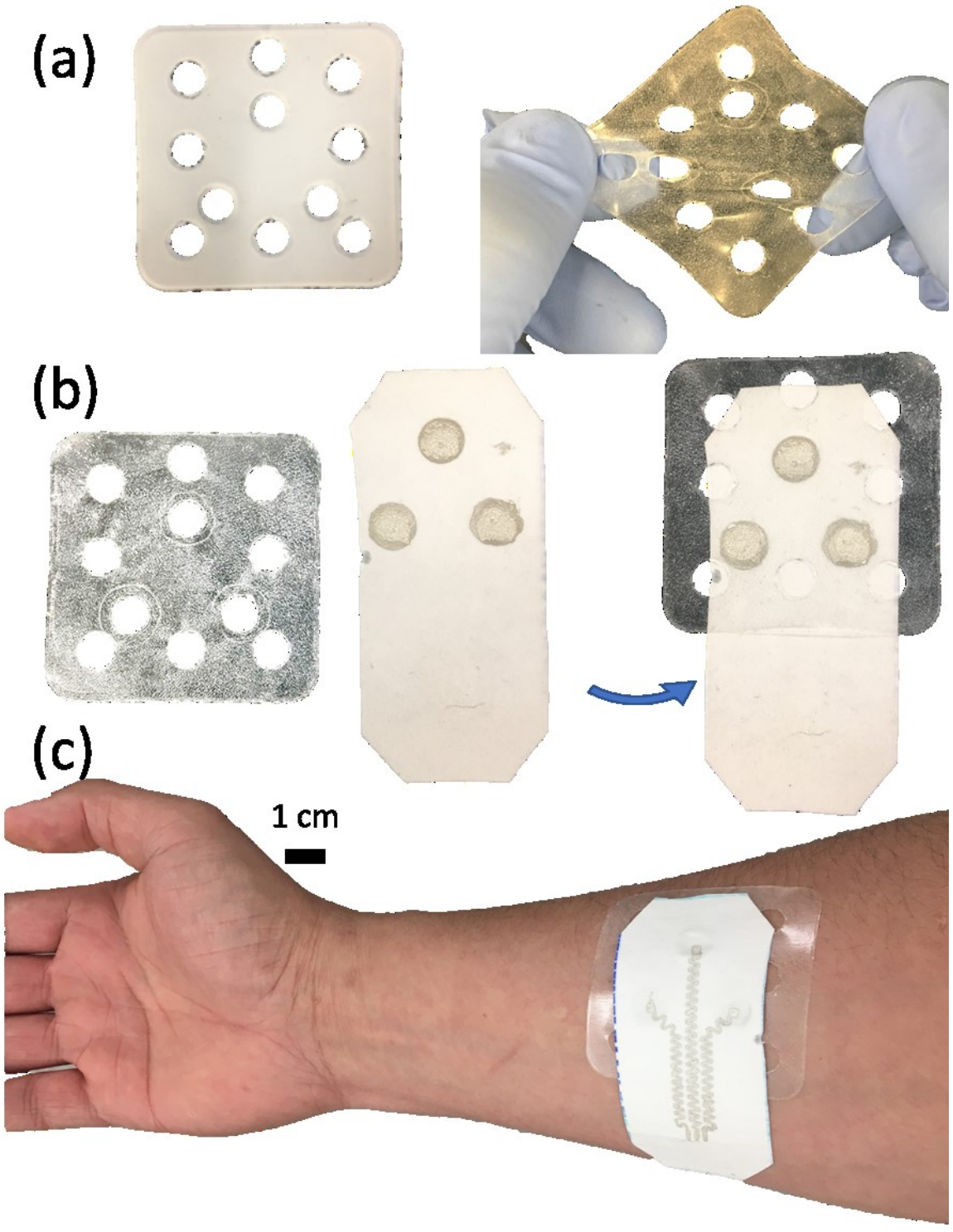

Figure 4.7. Schematic illustrating conformal attachment of e-textiles to skin by patterned medical adhesive. (a) The patterned adhesive (left: original, right: stretched), (b) attachment of the tape to the e-textile patch and (c) conformal adhesion of the e-textile patch to skin with the patterned double tape.

4.3.6 Fully Integrated E-Textile System for sEMG Application[3]

The two-layered e-textile patch was connected to an integrated electronic system that comprises a signal amplifier, a nose-reducing filter, an analogue to digital converter, and a Bluetooth wireless transmitter to export sEMG signals to data receiving electronics (Fig. 4.9 (a)). To attain a stable electrical connection between the e-textile patch and the circuit board, the e-textile patch was precisely aligned to connection pads on the circuit board, then clamped to the board (as shown in Fig. 4.8). The sEMG system is fully portable, lightweight, and compact. (Fig. 4.9 (b)). As sensing electrodes for sEMG, the two layered e-textile has an excellent merit of eliminating signal contamination because the location of serpentine traces is intrinsically insulated from by any skin-induced noises. In addition, the thin and conformal form factor of the e-textile further helps the suppression of unwanted artifacts from body movements, which are not associated with the electrical signals from the muscles of interest. Fig. 4.9 (c) demonstrates the block diagram of the integrated electronic system. Starting from the raw bipolar sEMG signal, the electronic system, amplified, filtered, biased, and digitized the signal at 1000 Hz, which was routed to a Bluetooth radio where it was transmitted in real-time to a computer for data analysis.

The signals from the sEMG patches were amplified with analog circuit to finely stay in the input voltage period of the analog-to-digital (A/D) converter. Then, the microcontroller regulated the converted signal and relay it to the Bluetooth transceiver. The wireless signal was sent to computer or mobile interfaces for further analysis of rehabilitation purposes. Here, the sEMG signal was

[3] The signal processing software for Section 3.3.6 is from Dylan K. Scott.

digitally processed to probe the actual muscle activities versus noise. Muscle activities measured by EMG signal are generally in the frequency range of 1-500 Hz, with the main frequency components concentrated in 60-150Hz.[101] Several factors such as muscle type, muscle activity, electrode-skin contact, electrode placements, fatigue and task duration affect timing and frequency characteristics of the sEMG signal.

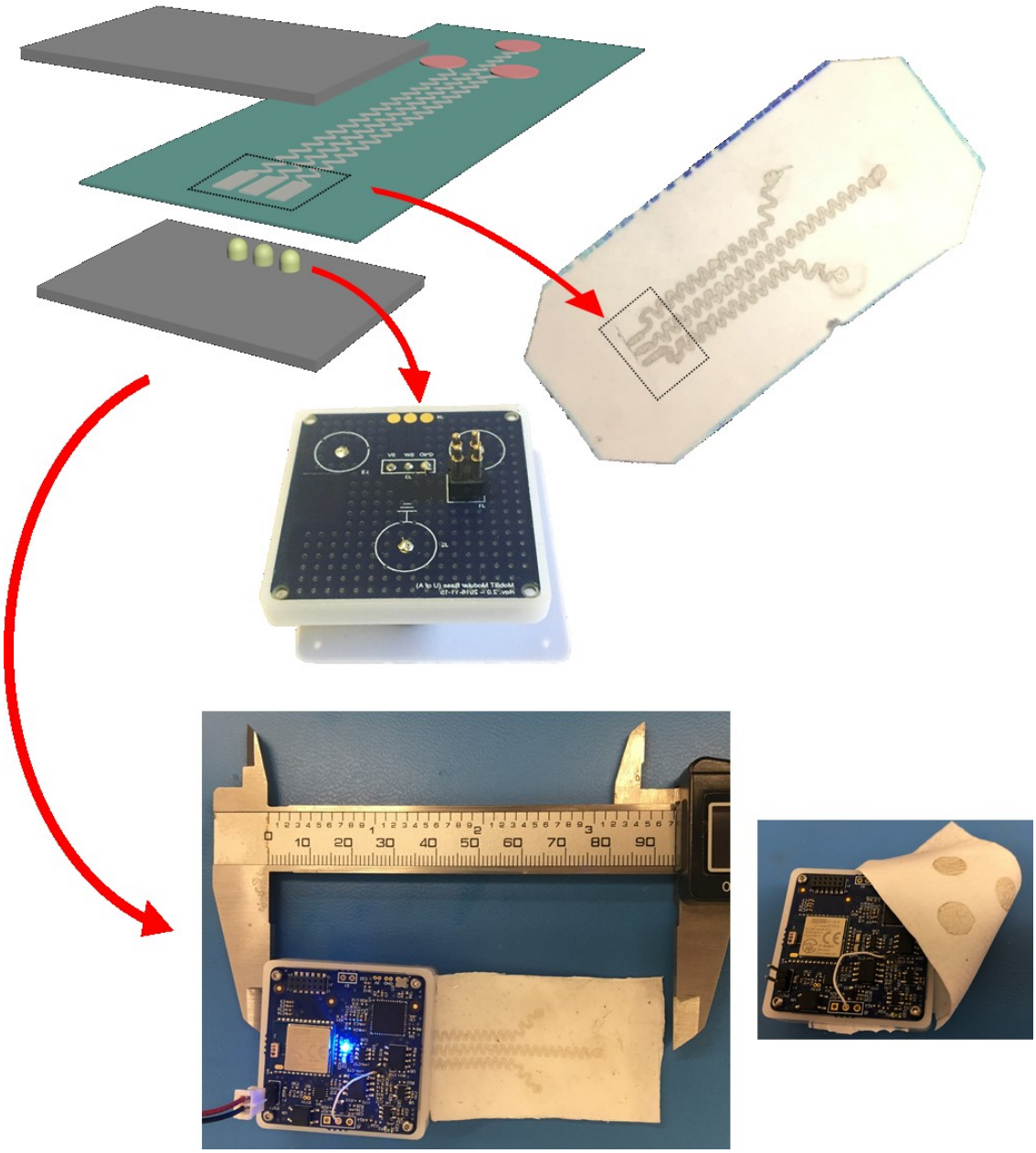

Figure 4.8. Schematic illustrates electrical connection of the e-textile and circuit board.

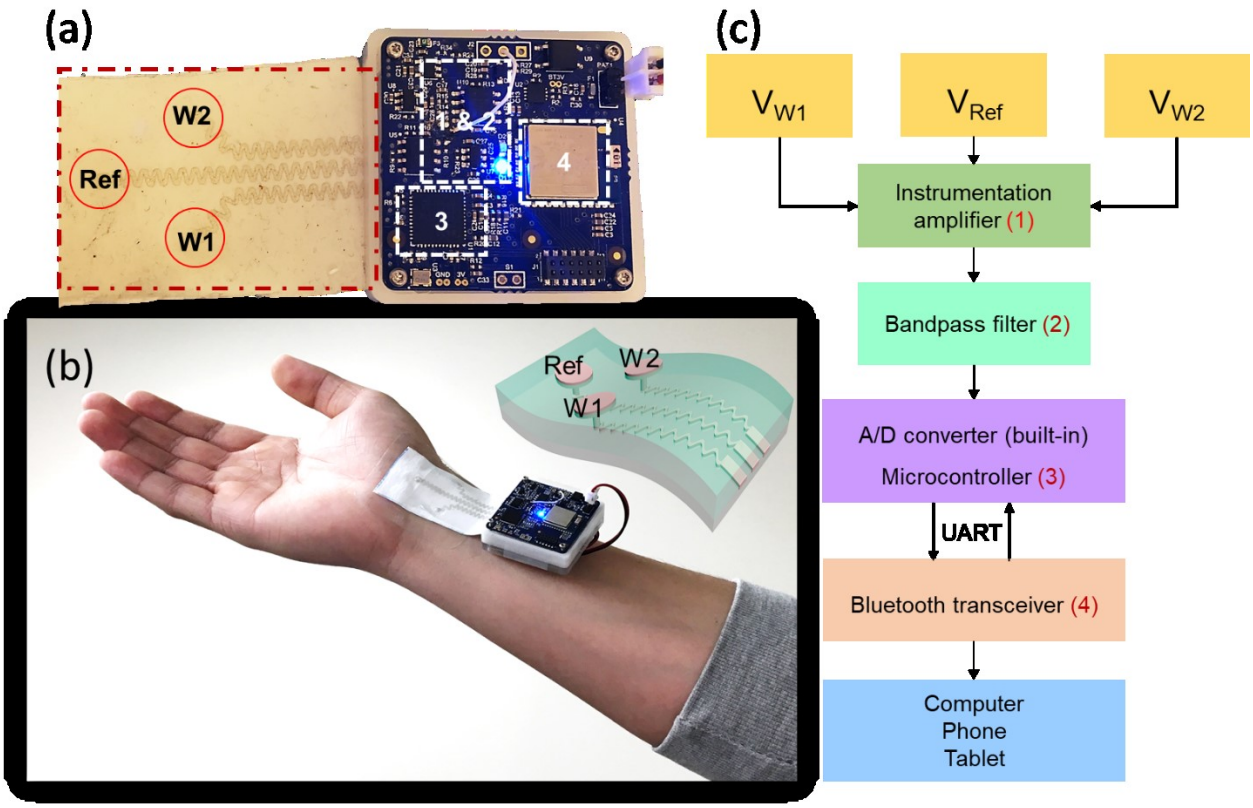

Figure 4.9. (a) Fully integrated sEMG sensor system with the two-layered e-textile sensing electrodes for real-time monitoring muscle activities. (b) Its placement on wrist muscle. (c) Block diagram of the electronics system.

4.3.7 sEMG Monitoring of Muscle Activities[4]

The sEMG system was worn on various body areas of a participant to monitor muscle activities from different parts of body, including (i) the submental space, (ii) elbow, (iii) calf, and (iv) ankle (Fig. 4.10 (a)). For each part, the reference electrode was located on or near a boney region while the remaining two electrodes were placed on the muscle belly of interest.[6] When necessary, the

[4] The signal processing software for Section 3.3.7 is from Dylan K. Scott.

system was secured with KT-tape® to the skin to prevent the detachment of the e-textile due to the weight of the system.

To place the sEMG system on the submental space, the reference electrode was placed on the body of the mandible while the other two electrodes were over the suprahyoid muscles separately during saliva swallowing, and mouth opening/closing [6]. The participant was asked to look straight ahead and swallow their saliva (5 trials). Thereafter, they were instructed to open and close their mouth (5 trials). While measuring the swallowing movements, positive and negative spikes occurred in the acquired signal (see in Fig. 4.10 (b) and (c)). Fig. 4.10 (d) and (f) show the signal during mouth opening and closing events. While the peak signals occurred in both activities, the sEMG patterns from the swallowing events were followed by a longer duration of signal undershoot (about 2-4 second) after the initial peak. In order to record the hand crunching events, the sEMG system was located on the elbow of the participant. The participant was asked to keep the hand closed and then crunch/relax. As shown in Fig. 4.10 (e) and (g), positive and negative peaks occurred during hand crunching and relaxing events, respectively. Similarly, the system attached on calf detected the signals from toe lifting (Fig. 4.10 (h) and (j)) and ankle bending (Fig. 4.10 (i) and (k)). In our work, an average moving filter and a band-pass filter (20 - 200 Hz) were used to process the raw sEMG signals, then median frequency between 1 - 500 Hz was calculated. We observed that the median frequencies of the sEMG signals were in the range of 60 – 150 Hz (See Fig. 4.10 (b) – (k)), which are in the frequency range of muscles activities as reported[101]. It indicates that the measured sEMG signal were representation of muscle electrical activities.

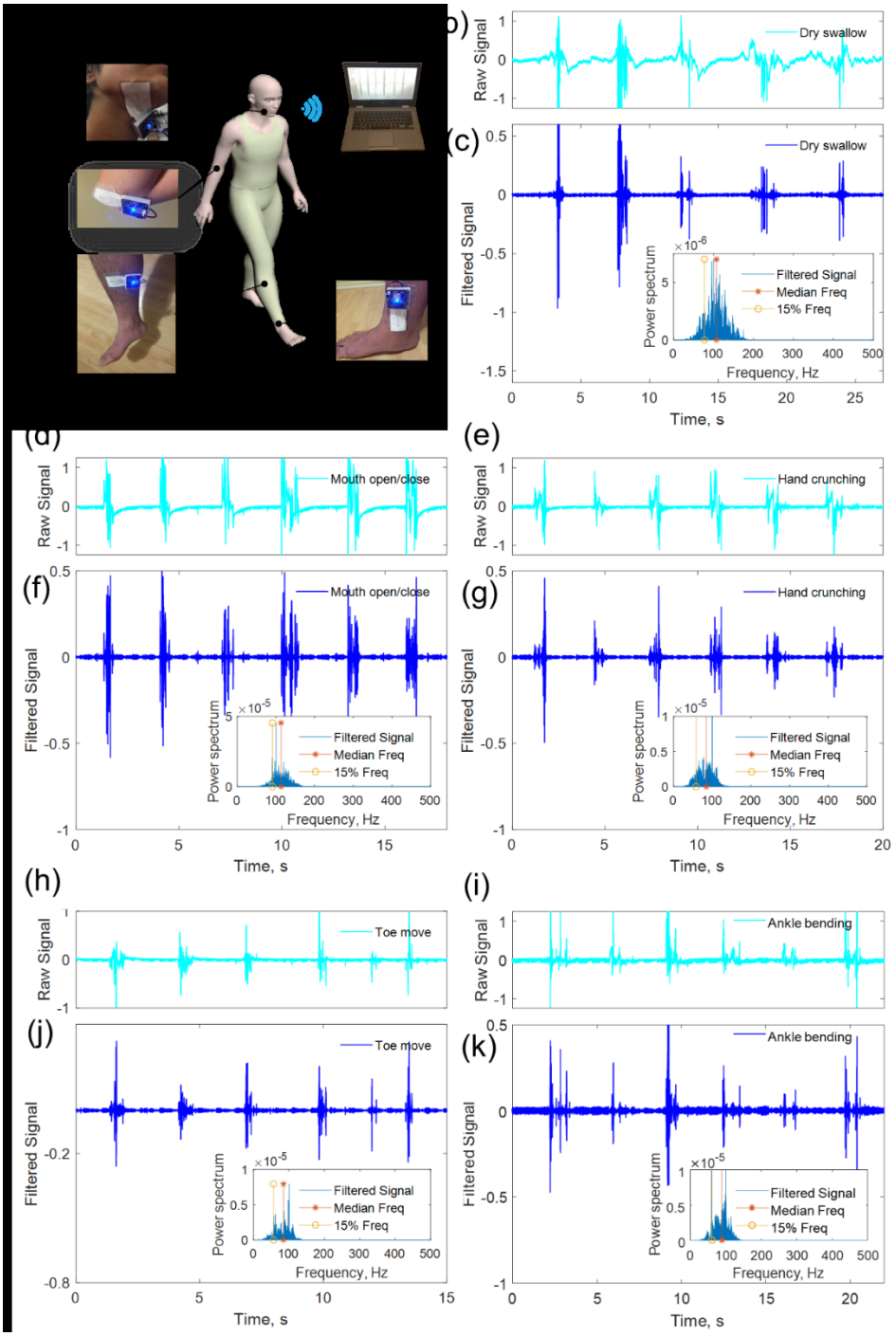

Figure 4.10. sEMG measurements of muscles activities. (a) Schematic illustration of sEMG measurements from various parts of human body. (b) The raw and (c) filtered sEMG signals from dry swallowing episodes measured from submental space. (d) The raw and (f) filtered sEMG signals from mouth open/close episodes measured from submental space. (e) The raw and (g) filtered sEMG signals from hand crunching episodes measured from elbow. (h) The raw and (j) filtered sEMG signals from toe lifting episodes measured from ankle. (i) The raw and (k) filtered sEMG signals from

ankle bending episodes measured from ankle. Here, all insets are power spectrums obtained by Fourier transforms of each data.

4.4 Conclusions

In this work, two-layered e-textile patches with high mechanical durability and electrical performance were fabricated by jet-printing Ag-powder/fluoropolymer-based nanocomposite ink on both sides of the porous textile substrate. The interplay between wetting and particle size effect controlled the thickness of the cladded-layer, where the dried inks coat the surfaces of the nanofibers inside of the porous textile substrate. The printed serpentine interconnects had a conductivity of ≈3000 S/cm. The reliability tests revealed that the increase in the resistance ratio value was ~5 times over 1,000 cycles of 30% uniaxial stretching. Controlling the thickness of the cladded-layer enabled the fabrication of two-layered e-textiles, which provided a remarkable advantage in designing electrodes for sEMG applications. With our custom-designed data acquisition/transmission electronics, a complete wireless sEMG system was successfully demonstrated. We anticipate that the design principles of our two-layered e-textiles will inspire new ways of engineering innovative, practical wearable health care systems.

Chapter 5. Stretchable, Mechanically and Electrically Robust E-Textiles by Controlling Ink Permeation and Nano-Fiber Encapsulation

5.1 Introduction

E-textiles, electronics-integrated textiles designed for ultimate comfort of wearers, provide an optimized platform for personalized healthcare devices[102],[103-105], as well as for other applications such as, textile batteries[106, 107], humidity sensors[108-110], and pressure-mapping systems[111-113]. For the wearer's comfort, stretchability of the e-textile system without compromising the performance of the electronic device is crucial, and this task can be done by connecting stretchable conductive interconnects between active functional devices[74, 114, 115]. Such stretchable interconnects have been realized by printed conductive polymers[116, 117], liquid metal filled elastomer channels[118, 119], and metal particle filled elastomer composites[73, 74, 76, 120] A representative example of such composite is a screen printed, silver particle filled fluoroelastomer traces on textile substrate with a sheet resistance of 0.06 Ωsq^{-1} by Someya and co-workers[74, 121]. We also recently developed two-layered e-textiles by controlling the permeation depth of jet-printed conductive ink that contains silver particles and fluoroelastomer and demonstrated the e-textile's efficacy as cutaneous electrodes to monitor electromyogram (EMG) and electroencephalogram (ECG)[122].

Coating a conductive layer on textile surface is also a popular method to achieve conductivity[123]. Such technology encompass a number of methods including dip coating[124, 125], spray coating[34], screen printing[120], and jet printing[126]. However, such approach often

compromises the stretchability of the textile. For example, electroless deposition of Ni on cotton yarns, followed by electrochemical deposition of RGO, allowed highly conductive charge collector for textile-based solid-state supercapacitor, however, the maximum strain of textile decreased by ~27% from pristine state[127]. There has been a report that an addition of PEDOT:PSS and graphene nanoflakes actually increases the stretchability of mercerized cotton.[128] However, for the use of stretchable interconnects, the conductive cotton exhibited rather high resistivity and modest stretchability of 25Ω/sq and 43%, respectively.

In Chapter 3, we show that, in certain cases, the stretchability (*i.e.* elongation at break) can significantly enhance by coating metal particle filled elastomer composites. Specifically, maximum uniaxial strain of a non-woven fibrous polyurethane nano-textile (up to 118% for a 270-μm-thick substrate) was significantly increased (up to 397%) by printing the composite ink layer (100 – 135 μm in total thickness of the ink) on one side. When the composite ink was printed, the ink solution permeated into the porous substrate, leading to the formation of conductive layer coated nanofibers (denoted as cladded-layer). The printed ink, composed of silver particles and fluoroelastomer, reinforced the polyurethane nanofibers to cause significant increase in stiffness and stretchability of the textiles. In addition, the permeation depth was found to be controlling factor to tune the stiffness of the printed textiles. Solvent selection and metal particle content affected the permeation of the ink and thus the mechanical properties of the printed textiles. The effect of applied pressure after printing was also studied. Electrical conductivity of the printed textiles was stable over 4000 cycles of 20% strain and release, which caused only twofold resistance increase.

5.2 Results and Discussion

The stretchable silver ink was fabricated through a simple and inexpensive method as mentioned in Chapter 3.2.1. The conductive composite ink consisted of a fluoroelastomer (DAI-EL G801, Daikin Industries) and silver particles (Sigma Aldrich, nominal average particle size of 2-3.5 μm, ≥99.9% trace metals basis) dissolved in butanone (Sigma Aldrich, M209-1), as shown in Fig. 5.1 (a). Initially, fluoroelastomer and butanone were mixed with a weight ratio of 1:2.55. After magnetic stirring for 6 hours, the silver particles were added to the solution. Here, the weight ratios between silver particles and fluoroelastomer were X:1, whereas X was 1.52, 2.36, and 3.55 for Ink-30%, Ink-40%, and Ink-50%, respectively. Then, the mixed solution was printed on top of nano-textile substrate (cross-section SEM image is shown in Fig. 5.2, Nanosan®-Sorb, Nanofiber Technology, LLC) by the nScrypt Tabletop-3Dn printer (Fig. 5.1 (b)). After printing with a nozzle of 150 μm diameter, selected samples were pressed for 10 minutes at controlled pressure values (Carver Hydraulic Unit Model #3912). All samples were then dried in a fume hood at room temperature for 8 hours.

Butanone played an important role for permeation of the composite ink into nano-textile because it swelled the nano-textile (Fig. 5.1 (d) and (e)) but did not degrade it (Fig. 5.3), thus facilitating the composite ink to permeate into the depth of the nano-textile substrate (Fig. 5.1 (c)). The composite ink permeated into the nano-textile via preferred wetting until the solvent evaporated.[122] Upon drying of the printed composite ink, the permeated portion of textiles form a cladded-layer on the surface of each polyurethane nanofiber (Fig. 5.1(f)).

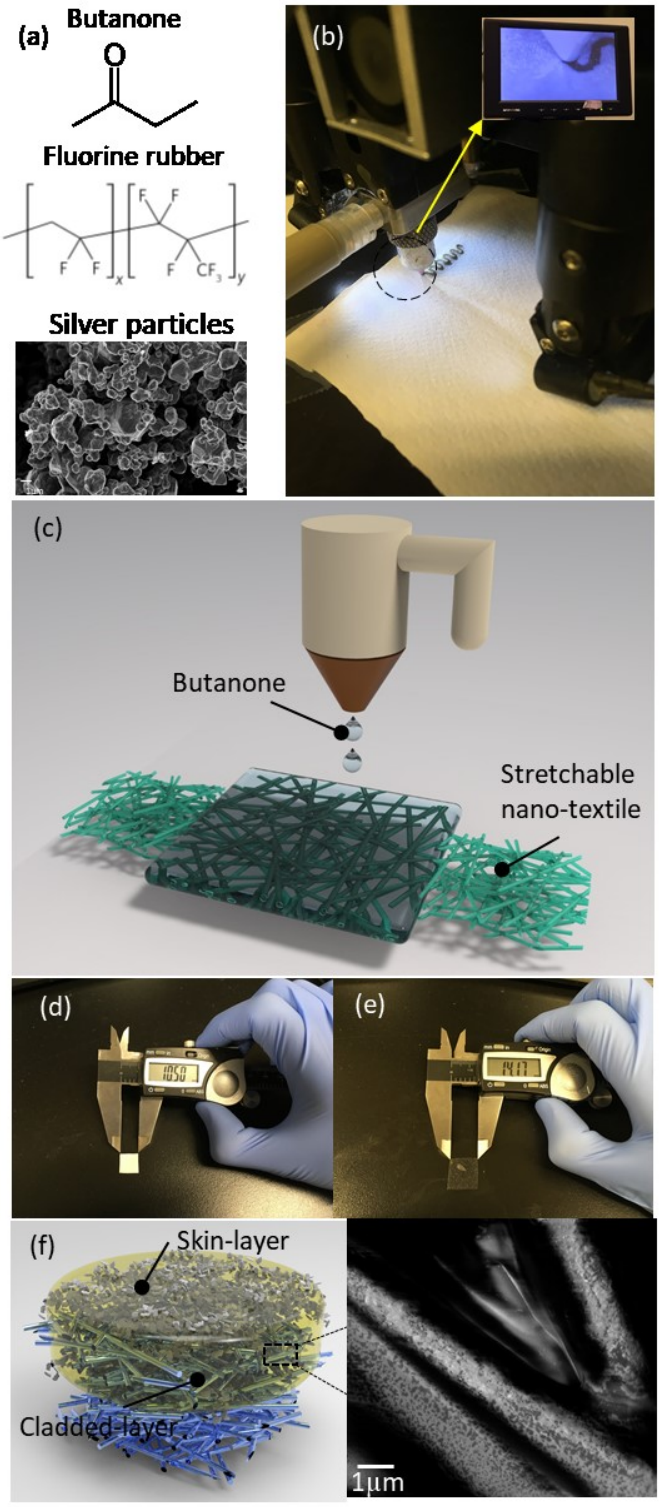

Fig. 5.1. (a) Ingredients of the conductive composite ink. (b) Our jet printer set up. (c) Schematic illustration showing that the solvent can cause localized swelling of the nano-textile substrate. Photos of nano-textiles (d) at pristine state and (e) at fully swollen state by immersing in butanone solvent. (f) Schematic illustration of a cross-sectional view of

the composite ink printed nano-textile. On the right side, a nanofiber coated with a cladded-layer is illustrated based on FESEM image that evidences the ink-coated strands in the printed nano-texile.

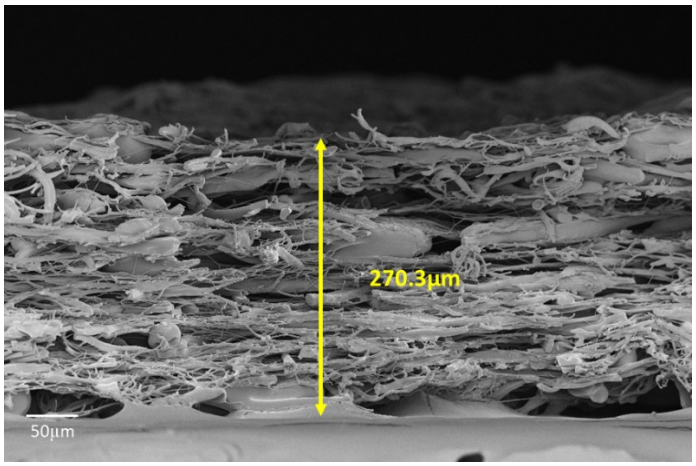

Fig. 5.2. Cross-section SEM image of pristine nano-textile.

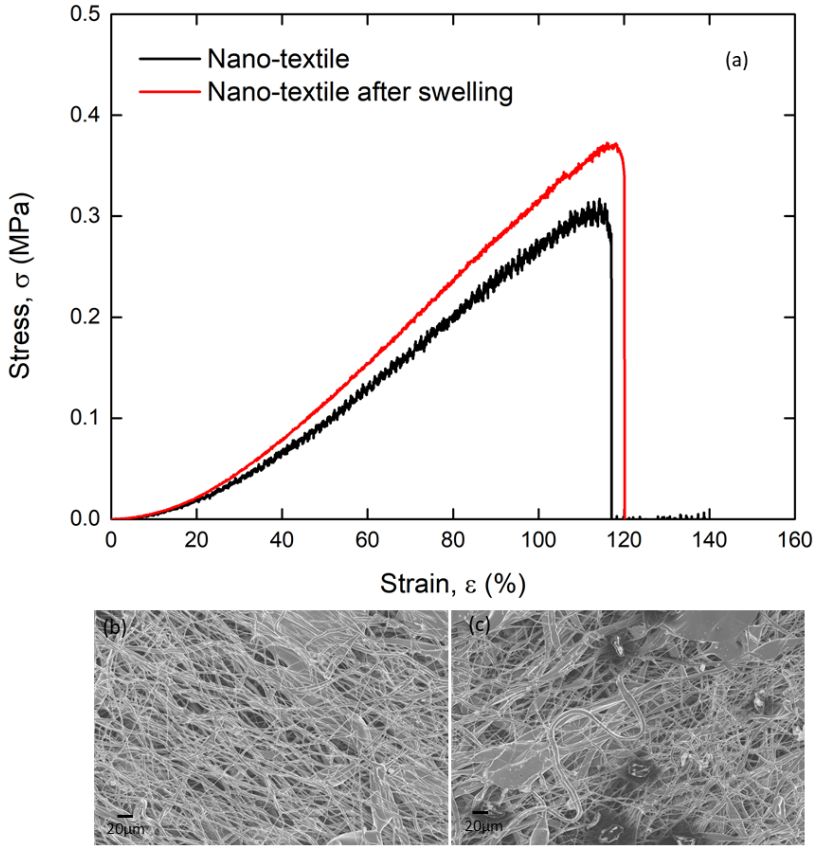

Fig. 5.3. (a) Stress-strain curves of pristine nano-textile and the nano-textile swelled by butanone and then dried (dried status after evaporating all butanone). Top-view SEM images of (b) pristine nano-textile, and (c) nano-textile swelled by butanone and then dried (dried status after evaporating all butanone).

The effect of silver concentration in the ink was investigated. Generally speaking, the ink viscosity increased with silver concentration, and thus caused a reduction of the permeation depth. Here, we printed rectangular patterns of 22 mm × 2.67 mm strips using Ink-30%, Ink-40% and Ink-50%, respectively. We compared their permeation depths, as shown in Fig. 5.4 (a), (b), and (c), respectively. As expected, the permeation depth decreased from 62.03 ± 1.07 μm to 47.51 ± 0.94 μm, then to 28.63 ± 1.29 μm as the silver concentration increased. The stress–strain behavior of these samples (ink cover the whole textile top surface) was tested with an Instron 5943 at a stretch rate of 10mm/min (Fig. 5.4 (d)). The strain to failure of pristine nano-textile and the three strip-printed nano-textiles was 118%, 264%, 248%, and 221%, respectively with increasing silver concentration. The Young's moduli of samples above were 0.387 MPa, 0.824 MPa, 1.413 MPa, and 2.292 MPa, respectively. This result is consistent with our hypothesis that the cladded-layer of silver/fluoroelastomer on each strand of nanofibers reinforced the nano-textile, and thus both the strain-to-failure and the stiffness values increased with the penetration depth.

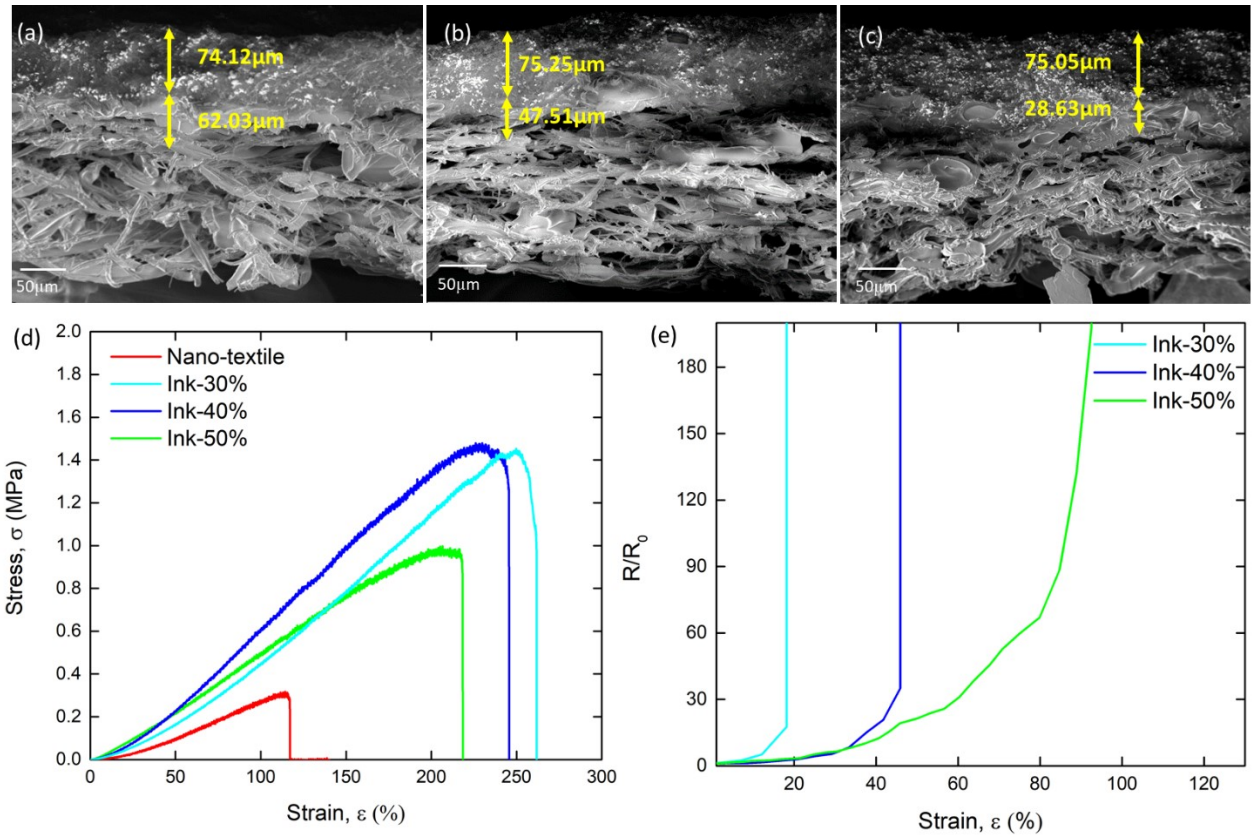

Fig. 5.4. Effect of silver particle concentration in the ink. Cross-section SEM images of the printed textiles with a) Ink-30%, b) Ink-40%, and c) Ink-50%. d) Stress-strain curves of pristine and the three strip-printed nano-textiles. e) Normalized electrical resistance versus strain for the three strip-printed nano-textile during the tensile test.

In order to validate our hypothesis that the cladded-layer of silver/fluoroelastomer reinforced the mechanical properties of the nano-textile, we performed a tensile test of free-standing fluoroelastomer, ink-30%, ink-40% and ink-50% (Fig. 5.5). Here, the Young's modulus values were 0.998 MPa, 1.231 MPa, 1.945 MPa, and 3.324 MPa, respectively, where the trend was consistent with the Young's moduli of strip-printed nano-textile samples. Most probably, this trend implies that the Young's modulus, which is determined at relatively low strain range, is dominated by the ~75 µm-thick dried-ink 'skins' shown in Fig. 5.4 (a)-(c). The trend shown in the strain-to-failure of the free-standing samples – 1833 %, 1345 %, 266 %, and 157 % for fluoropolymer, Ink-

30%, Ink-40%, and Ink-50%, respectively – shows a similar trend in the strip-printed nano-textile samples. This is because the fluoroelastomer offers high stretchability when it is cladded inside nano-porous of the nano-textile.

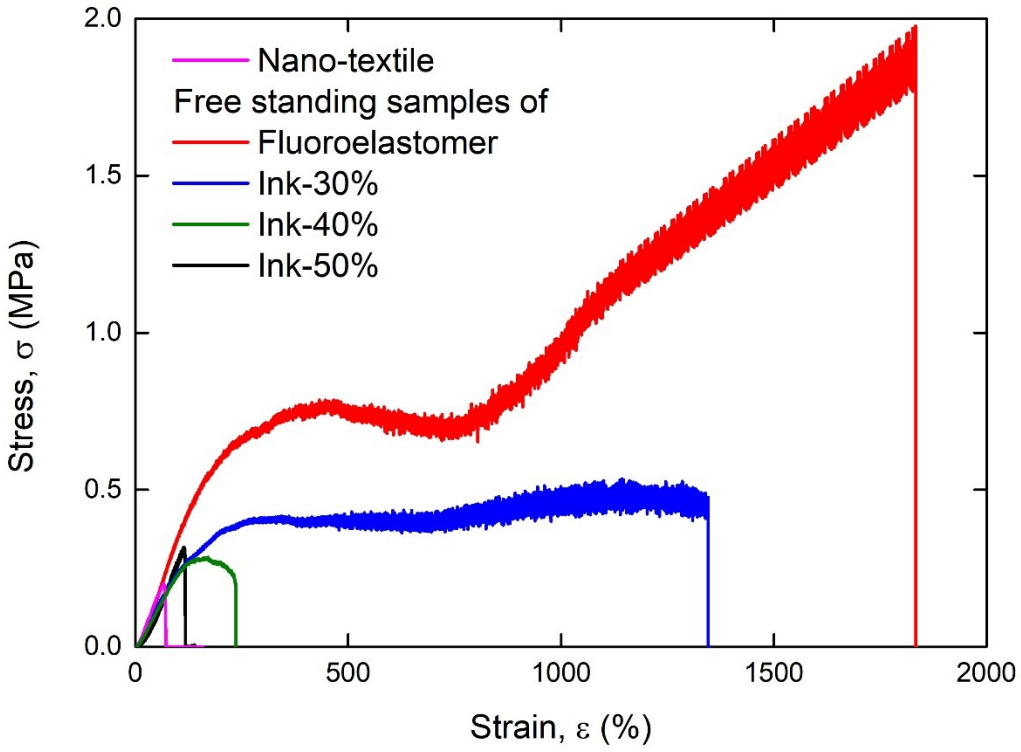

Fig. 5.5. Stress-strain curves of free-standing samples of pristine fluoroelastomer and the three inks with different concentration.

The electrical conductivity increased with increasing silver particle content in the ink solution (which is in decreasing order in terms of penetration depth). The conductivity of Ink-30%, Ink-40% and Ink-50% strips, measured by a Keithley 2400 SourceMeter, were 81.39 $S \cdot cm^{-1}$, 1104.43 $S \cdot cm^{-1}$ and 3399.7 $S \cdot cm^{-1}$, respectively. This is because of the effect of silver particle density in dried ink. Ink-50%, with a volume fraction of 37.86% containing the highest silver particle density, can

result in the highest conductivity, while Ink-30% and Ink-40% only contain 20.47% and 28.82% volume fraction of silver particles, respectively.

The effect of uniaxial stretching on the electrical conductivity is shown in Fig. 5.4 (e). Ink-30% and Ink-40% showed poor electrical conductivity, whereas breakdowns occurred at 20% and 46% strain, respectively. Ink-50%, on the other hand, showed a similar trend with Ink-40% up to 35% strain whereas a catastrophic breakdown did not happen until up to 92% strain, with good recovery under 50% strain.

A pressing treatment[74] (*i.e.*, applying compressive pressure for 10 minutes without applying heat) was investigated to further improve mechanical and electrical properties of the printed textiles. Here, it is important to understand that the pressing was done 5 minutes after printing; in other words, the printed region of the nano-textile substrate was still wet and swollen with the solvent. Firstly, we evaluated the structural compression resilience limit of pristine nano-textiles. The nano-textile substrate could retain its original thickness after removing the pressure when the applied pressure was up to 2280 kPa (Fig. 5.6 (c)). However, the electrical conductivities of the strip-printed textiles were irreversibly degraded when the applied pressure reached ~53 kPa (Fig. 5.6 (c)). Thus, we compared the effect of applied pressures of 10 kPa and 50 kPa on the Ink-50% printed nano-textiles. Before pressing, the permeation depth was 28.63 $\pm$ 1.29 μm with a strong presence of ~75 μm-thick dried ink 'skin' at the top. After pressing, the permeation depth was significantly increased as shown by SEM images in Fig. 5.6 (a) and (b). The silver particle permeated into nano-textile 105 $\pm$ 0.89 μm at pressure of 10 kPa and 156.3 $\pm$ 0.49 μm at pressure of 50 kPa. The strain to failure with applied pressures of 10 kPa and 50 kPa were increased to 306% and 397%, respectively, compared to the without-pressure value of 221% (Fig. 5.6 (d)). At the same time, the tensile moduli decreased from 2.292 MPa to 1.622 MPa, then to 0.694 MPa, with

increasing applied pressures from zero to 10 kPa, then to 50 KPa. The strain tolerance for electrical conductivity was significantly improved (Fig. 5.6 (e)). It still had conductivity of 339S/cm at 70%strain. Other researchers' work was listed as comparison in Table 2. These improved mechanical and electrical properties with applied pressure are possibly due to the combination of an altered structures of nano-strands in the e-textile (tearing and fusion of the strands) and increased permeation depth of the cladded-layer.

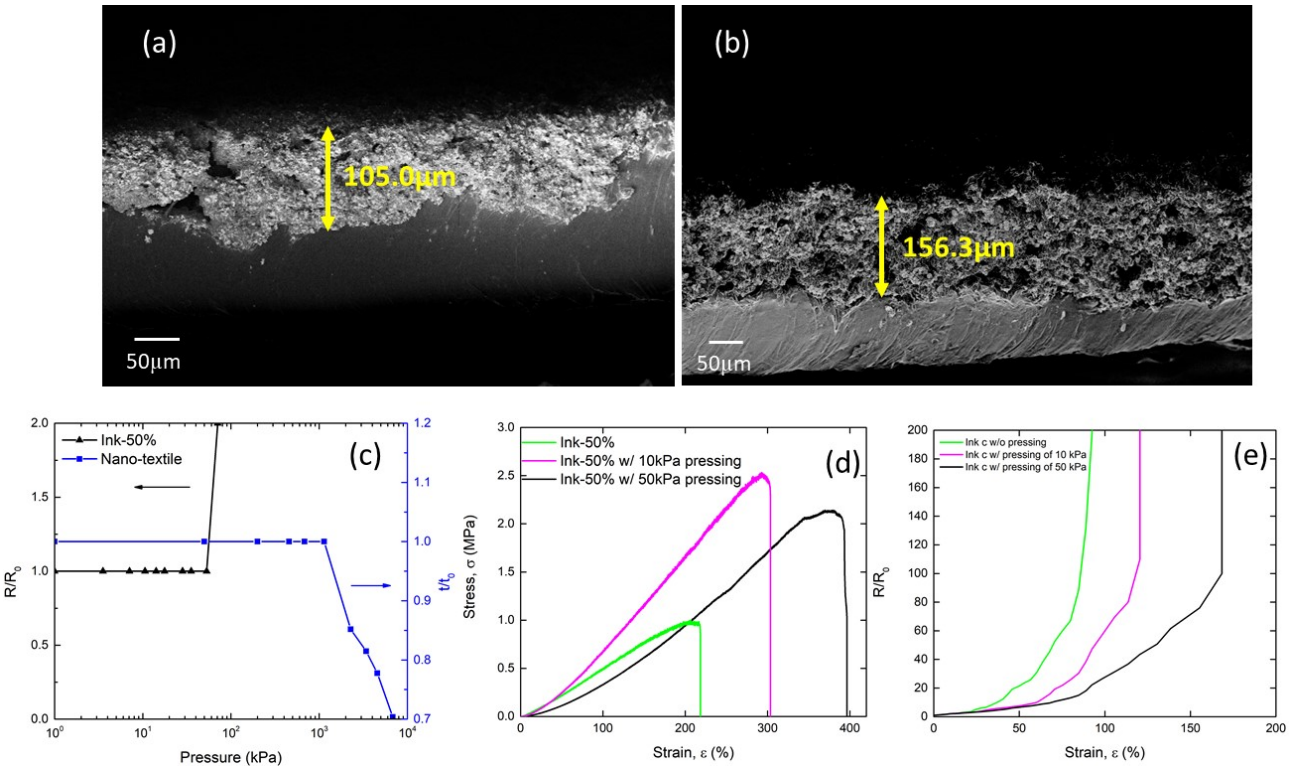

Fig. 5.6. The effect of pressing treatment on the structural, mechanical, and electrical properties of Ink-50% printed nano-textile. Cross-section SEM images of samples with applied pressures of (a) 10kPa and (b) 50kPa. (c) The thickness resilience (i.e. thickness after applied pressure normalized by the initial thickness) of a pristine nano-textile (blue square) and the normalized electrical resistance of an Ink-50% printed nano-textile (black triangle) plotted against applied pressures. (d) Stress-strain curves and (e) normalized resistance changes of Ink-50% printed nano-textiles with different applied pressures.

Finally, we investigated the durability of the Ink-50% printed nano-textile with 50 kPa pressing treatment over the repeated stress of stretch/release cycles. A close-up view of the first 5 cycles of 30% strain exhibited a minor, but gradual, degradation of zero-strain resistance values (Fig. 5.7 (a)). The resistance change after 4000 cycles of 20% strain is still less than 2.5 times (Fig. 5.7 (b)). Such durability over stretch/release cycles with remarkably high conductivity value (~1400 $S \cdot cm^{-1}$ after 4000 cycles of 20% stretch) evidences the efficacy of the printed nano-textiles for conductive traces in e-textile systems.

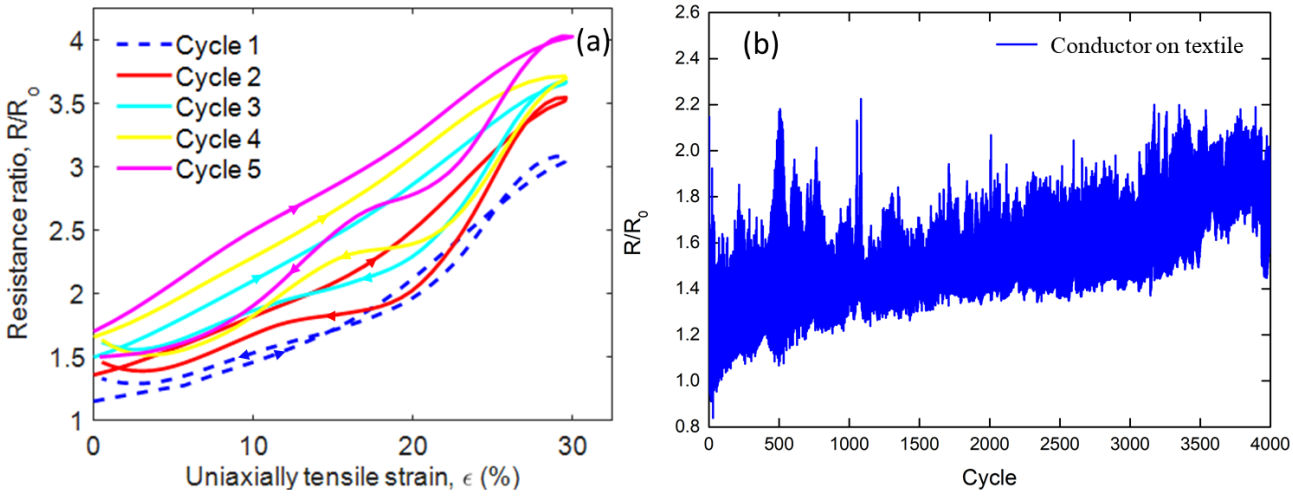

Fig. 5.7. Normalized electrical resistance changes of the Ink-50% printed and 50 kPa-pressed sample (a) during the first 5 stretch/release cycles with 30% maximum strain and (b) during 4000 cycles with 20% maximum strain.

5.3 Conclusion

In conclusion, we fabricated mechanically and electrically robust stretchable e-textiles by permeating fluoroelastomer-based silver particle composite ink into the pores of nano-textile substrate. The interplay between wetting and drying of the composite inks, as well as the solvent-induced swelling of nano-textile substrate, controlled the permeation depth of the ink into the porous textile substrate. The permeation depth was 28.63 μm, 47.51 μm, and 62.03 μm for Ink-

50%, Ink-40%, and Ink-50% respectively, whereas the overall thickness of the nano-textile substrate is ~270 μm. Moreover, the cladded-layer formed by encapsulating nano-fibers with silver particles and fluoroelastomer significantly enhanced its strain-to-failure behaviours due to intrinsically stronger and tougher fluoroelastomer compared to polyurethane-based nano-fibrous substrate. Pressing at 50 kPa for 5 minutes further facilitated the permeation of fluoroelastomer throughout the nano-textile, resulted in the strain-to-failure value of 397%, which is a big improvement compared to 118% of pristine nano-textile. The silver conductor had an initial conductivity of 3399.7 $S \cdot cm^{-1}$ and its relative resistance change is only around 2.5 times after 4000 cycles stretching tests of 20% strain. This mechanically and electrically robust e-textile can provide more opportunities for wearable biosensors and many other internet-of-things applications.

Chapter 6. Conclusion

This work attempts to develop novel techniques for fabricating wearable healthcare sensors, and more specifically, focusing on developing sEMG sensing devices. We developed a simple wax-printing technique to fabricate conductive features on flexible and conformal substrate. Furthermore, we fabricated a stretchable silver ink and developed e-textile patches for sEMG systems. The textile substrate offers high conformability, stretchability and breathability to our device.

Start with Chapter 1, a review of current EMG sensing systems was carried out. The difference between intramuscular EMG and surface EMG was discussed. Challenges and problems with current sEMG systems were described.

In Chapter 2, a review of the field of printing technology for fabricating flexible and stretchable electronics was carried out. The advantages and disadvantages of different printing technology were compared and discussed including microcontact printing, transfer printing, spray printing, screen printing and inkjet printing. Specifically, the working principle of nScrypt printing technique was described. We also discussed the ink drop filtration model and surface energy model. Finally, we did a literature review of current silver inks and listed their advantages and limitations.

Chapter 3 described a simple and cost-effective wax-printing technique for fabricating flexible circuit boards and sensors. The commercial and printable wax was used as a lift-off mask and it can be removed easily with boiling water. The Cr/Au layer was sputtered onto the substrate as conductive interconnects. The resistance of the conductive interconnects only increased 1.05

times after 20,000 cyclic compression tests at ~7 MPa pressure. The resolution of our technique can reach 0.1 mm. The multilayered flexible system for sEMG sensor was designed, fabricated, and fully electrical integrated. The reusable adhesive silicone gel was used as adhesive layer to realize seamlessly following the contour of curvilinear skin topology. The saliva swallow signals were measured and transmitted to laptop with our sEMG device. These proved that our wax-printing technique with simple fabrication procedures can be a promising pathway towards flexible circuit boards.

In Chapter 4, an e-textile was developed with improved mechanical durability and electrical performance by jet-printing a nanocomposite ink onto polyurethane-based nano-textile. The printed serpentine interconnects had a conductivity of ~3000 S/cm. Their resistance ratio only increased up to 5 times over 1000 cyclic stretching under 30% uniaxial strain. Moreover, a two-layered design was achieved by simply injecting small amount of ink with a needle connect top and bottom layer. The e-textile was used to fabricate a fully printed, two-layered, stretchable electronic system for sEMG application. The sEMG system can record muscle activities of dry swallow, mouth open/close, hand crunching, toe move, and ankle bending. We believe that the e-textile with nanocomposite ink in couple to nano-textile can open new opportunities of engineering innovative, practical wearable healthcare.

In Chapter 5, further investigation on the mechanical properties of the e-textile was carried out. Butanone was selected as the solvent to swell the polyurethane-based nano-textile resulting in deep permeation of silver ink in the nano-textile. Moreover, the relation between permeation depth and ink concentration was studied. Ink with lower concentration exhibited lower viscosity resulting in deeper permeation. However, the conductivity of ink with low concentration is lower than the ink with high concentration. We also figured out that pressing process could cause

deeper permeation. The optimal pressure was investigated to achieve deep permeation without destroying the textile as well as conductive interconnects. Meanwhile, the cladded-layer was formed by encapsulation of silver particles on nano-fibers. Such cladded-layers significantly improved the mechanical properties of e-textile. The strain to failure of the e-textile increased 3 times in comparison to the pristine nano-textile. The resistance change was less than 2.5 times after 4000 cycles of 20% strain.

Overall, a simple and cost-effective wax-printing technique was developed for flexible circuit boards fabrication and a stretchable silver ink for ink-jet printing to fabricate stretchable e-textiles was studied. Furthermore, the swelling mechanism and cladding phenomenon which can mechanically strengthen our e-textile were investigated. Finally, with the custom-developed electronic circuits, a sEMG system with wireless data transmission in demonstrated. Since textiles are inherently “smart materials” with several unique characteristics that have been optimized for human comfort over thousands of years, it is anticipated that our e-textiles will be effective in healthcare and sports applications.

References

1. Gupta, S., et al., *Device modelling for bendable piezoelectric FET-based touch sensing system.* IEEE Transactions on Circuits and Systems I: Regular Papers, 2016. **63**(12): p. 2200-2208.
2. Dahiya, R.S. and M. Valle, *Robotic tactile sensing: technologies and system*. 2012: Springer Science & Business Media.
3. Wang, X., Z. Liu, and T. Zhang, *Flexible Sensing Electronics for Wearable/Attachable Health Monitoring.* Small, 2017.
4. Jin, H., Y.S. Abu-Raya, and H. Haick, *Advanced Materials for Health Monitoring with Skin-Based Wearable Devices.* Adv Healthc Mater, 2017.
5. Gao, W., et al., *Fully integrated wearable sensor arrays for multiplexed in situ perspiration analysis.* Nature, 2016. **529**(7587): p. 509-14.
6. Constantinescu, G., et al., *Epidermal electronics for electromyography: An application to swallowing therapy.* Medical engineering & physics, 2016. **38**(8): p. 807-812.
7. Jamal, M.Z., *Signal acquisition using surface EMG and circuit design considerations for robotic prosthesis*, in *Computational Intelligence in Electromyography Analysis-A Perspective on Current Applications and Future Challenges*. 2012, InTech.
8. De Luca, C.J., *The use of surface electromyography in biomechanics.* Journal of applied biomechanics, 1997. **13**(2): p. 135-163.
9. De Luca, C., *Electromyography.* Encyclopedia of Medical Devices and Instrumentation, 2006.
10. Heo, J.S., Y.-H. Kim, and S.K. Park, *Recent Progress of Textile-Based Wearable Electronics: A Comprehensive Review of Materials, Devices, and Applications.* Small, 2017. **14**(3): p. 1703034.
11. Wang, X., Z. Liu, and T. Zhang, *Flexible Sensing Electronics for Wearable/Attachable.* Small, 2017. **13**(25): p. 1602790.
12. Stoppa, M. and A. Chiolerio, *Wearable Electronics and Smart Textiles: A Critical Review.* Sensors, 2014. **14**: p. 11957-11992.
13. Bae, H., et al., *Functional Circuitry on Commercial Fabric via Textile-Compatible Nanoscale Film Coating Process for Fibertronics.* Nano Letters, 2017. **17**(10): p. 6443–6452.
14. Yu, A., et al., *Core–Shell-Yarn-Based Triboelectric Nanogenerator Textiles as Power Cloths.* ACS Nano, 2017. **11**: p. 12764−12771.
15. Di, J., et al., *Carbon-Nanotube Fibers for Wearable Devices and Smart Textiles.* Advanced Materials, 2016. **28**: p. 10529-10538.
16. Jost, K., et al., *Knitted and screen printed carbon-fiber supercapacitors for applications in wearable electronics.* Energy & Environmental Science, 2013. **6**: p. 2698-2705.
17. Cherenack, K., et al., *Woven Electronic Fibers with Sensing and Display Functions for Smart Textiles.* Advanced Materials, 2010. **22**(45): p. 5178-5182.
18. Huang, Y., et al., *From Industrially Weavable and Knittable Highly Conductive Yarns to Large Wearable Energy Storage Textiles.* ACS Nano, 2015. **9**(5): p. 4766–4775.
19. Maccioni, M., et al., *Towards the textile transistor: Assembly and characterization of an organic field effect transistor with a cylindrical geometry* Applied Physics Letters, 2006. **89**: p. 143515.
20. Yoon, S.S., et al., *Highly Conductive Graphene/Ag Hybrid Fibers for Flexible Fiber-Type Transistors.* Scientific Reports, 2015. **5**: p. 16366.
21. Rossi, D.D., *Electronic Textiles: A Logical Step.* Nature Materials 2007. **6**: p. 329.

22. Hamedi, M., R. Forchheimer, and O. Inganäs, *Towards woven logic from organic electronic fibres.* Nature Materials, 2007. **6**: p. 357-362.
23. Xie, J., H. Long, and M. Miao, *High sensitivity knitted fabric strain sensors.* Smart Materials and Structures, 2016. **25**: p. 105008.
24. Ryu, S., et al., *Extremely Elastic Wearable Carbon Nanotube Fiber Strain Sensor for Monitoring of Human Motion.* ACS Nano, 2015. **9**(6): p. 5929–5936.
25. Wu, X., et al., *Highly Sensitive, Stretchable, and Wash-Durable Strain Sensor Based on Ultrathin Conductive Layer@Polyurethane Yarn for Tiny Motion Monitoring.* ACS Applied Materials & Interfaces, 2016. **8**(15): p. 9936-9945.
26. Wang, C., et al., *Carbonized Silk Fabric for Ultrastretchable, Highly Sensitive, and Wearable Strain Sensors* Advanced Materials, 2016. **28**(31): p. 6640-6648.
27. Zysset, C., et al., *Textile Integrated Sensors and Actuators for near-Infrared Spectroscopy.* Optics Express, 2013. **21**: p. 3213–3224.
28. Yang, Y.-L., et al., *Thick-Film Textile-Based Amperometric Sensors and Biosensors.* Analyst, 2010. **135**: p. 1230-1234.
29. Kim, K.N., et al., *Highly Stretchable 2D Fabrics for Wearable Triboelectric Nanogenerator under Harsh Environments.* ACS Nano, 2015. **9**(6): p. 6394-6400.
30. Zhang, Z., et al., *Facile Method and Novel Dielectric Material Using a Nanoparticle-Doped Thermoplastic Elastomer Composite Fabric for Triboelectric Nanogenerator Applications.* ACS Applied Materials & Interfaces, 2018.
31. Zeng, W., et al., *Highly durable all-fiber nanogenerator for mechanical energy harvesting* Energy & Environmental Science, 2013. **6**: p. 2631-2638
32. Seung, W., et al., *Nanopatterned Textile-Based Wearable Triboelectric Nanogenerator.* ACS Nano, 2015. **9**(4): p. 3501-3509.
33. Zhong, J., et al., *Fiber-Based Generator for Wearable Electronics and Mobile Medication.* ACS Nano, 2014. **8**(6): p. 6273-6280.
34. Le, V.T., et al., *Coaxial fiber supercapacitor using all-carbon material electrodes.* ACS nano, 2013. **7**(7): p. 5940-5947.
35. Meng, Q., et al., *Thread‐like Supercapacitors Based on One‐Step Spun Nanocomposite Yarns.* Small, 2014. **10**(15): p. 3187-3193.
36. Harnett, C.K., H. Zhao, and R.F. Shepherd, *Stretchable Optical Fibers: Threads for Strain-Sensitive.* Advanced Materials Technologies, 2017. **2**(9): p. 1700087.
37. Cottet, D., et al., *Electrical characterization of textile transmission lines.* IEEE Trans. Adv. Packag., 2003. **26**: p. 182-190.
38. Bhat, N.V., D.T. Seshadri, and S. Radhakrishnan, *Preparation, Characterization, and Performance of Conductive Fabrics: Cotton + PANi* Textile Research Journal, 2004. **74**(2): p. 155-166.
39. Yoon, J., et al., *Robust and stretchable indium gallium zinc oxide-based electronic textiles formed by cilia-assisted transfer printing.* Nature Communications, 2016. **7**: p. 11477.
40. Matsuhisa, N., et al., *Printable elastic conductors with a high conductivity for electronic textile applications.* Nature Communications, 2015. **6**: p. 7461.
41. Jin, H., et al., *Enhancing the Performance of Stretchable Conductors for E‐Textiles by Controlled Ink Permeation.* Advanced Materials, 2017. **29**: p. 1605848.
42. Richards, H.R., *Thermal Degradation of Fabrics and Yarns - Part I: Fabrics.* Journal of the Textile Institute, 1984. **75**(1): p. 28-36.
43. Khan, S., et al., *Flexible tactile sensors using screen-printed P (VDF-TrFE) and MWCNT/PDMS composites.* IEEE Sens. J, 2015. **15**(6): p. 3146-3155.
44. Grimes, A., et al., *Shrinky-Dink microfluidics: rapid generation of deep and rounded patterns.* Lab on a Chip, 2008. **8**(1): p. 170-172.

45. Nie, X., H. Wang, and J. Zou, *Inkjet printing of silver citrate conductive ink on PET substrate.* Applied surface science, 2012. **261**: p. 554-560.
46. Harriott, L.R., *Limits of lithography.* Proceedings of the IEEE, 2001. **89**(3): p. 366-374.
47. Wu, H., et al., *Patterning Hydrophobic Surfaces by Negative Microcontact Printing and Its Applications.* Small, 2018. **14**(38): p. 1802128.
48. Secor, E.B., et al., *Gravure printing of graphene for large‐area flexible electronics.* Advanced materials, 2014. **26**(26): p. 4533-4538.
49. Hyun, W.J., et al., *High‐resolution patterning of graphene by screen printing with a silicon stencil for highly flexible printed electronics.* Advanced Materials, 2015. **27**(1): p. 109-115.
50. Hyun, W.J., et al., *All‐Printed, Foldable Organic Thin‐Film Transistors on Glassine Paper.* Advanced Materials, 2015. **27**(44): p. 7058-7064.
51. Secor, E.B., et al., *Inkjet printing of high conductivity, flexible graphene patterns.* The journal of physical chemistry letters, 2013. **4**(8): p. 1347-1351.
52. Béduer, A., et al., *A simple and versatile micro contact printing method for generating carbon nanotubes patterns on various substrates.* Microelectronic Engineering, 2012. **97**: p. 301-305.
53. Abdelhalim, A., et al., *Fabrication of carbon nanotube thin films on flexible substrates by spray deposition and transfer printing.* Carbon, 2013. **61**: p. 72-79.
54. Davis, J.R., *Handbook of thermal spray technology*. 2004: ASM international.
55. Soukup, R., A. Hamáček, and J. Řeboun. *Organic based sensors: Novel screen printing technique for sensing layers deposition*. in *Electronics Technology (ISSE), 2012 35th International Spring Seminar on*. 2012. IEEE.
56. Jabbour, G.E., R. Radspinner, and N. Peyghambarian, *Screen printing for the fabrication of organic light-emitting devices.* IEEE Journal of selected topics in quantum electronics, 2001. **7**(5): p. 769-773.
57. Liang, J., K. Tong, and Q. Pei, *A water‐based silver‐nanowire screen‐print ink for the fabrication of stretchable conductors and wearable thin‐film transistors.* Advanced Materials, 2016. **28**(28): p. 5986-5996.
58. Zhuang, J.L., et al., *Patterned Deposition of Metal‐Organic Frameworks onto Plastic, Paper, and Textile Substrates by Inkjet Printing of a Precursor Solution.* Advanced Materials, 2013. **25**(33): p. 4631-4635.
59. Colasanti, S., V.D. Bhatt, and P. Lugli. *3D modeling of CNT networks for sensing applications*. in *Ph. D. Research in Microelectronics and Electronics (PRIME), 2014 10th Conference on*. 2014. IEEE.
60. https://www.nscrypt.com/.
61. Li, B., P.A. Clark, and K. Hail, *Robust printing and dispensing solutions with three sigma volumetric control for 21st century manufacturing and packaging.* MRS Online Proceedings Library Archive, 2007. **1002**.
62. Pack, M., et al., *Colloidal drop deposition on porous substrates: competition among particle motion, evaporation, and infiltration.* Langmuir, 2015. **31**(29): p. 7953-7961.
63. Lembach, A.N., et al., *Drop impact, spreading, splashing, and penetration into electrospun nanofiber mats.* Langmuir, 2010. **26**(12): p. 9516-9523.
64. Washburn, E.W., *The dynamics of capillary flow.* Physical review, 1921. **17**(3): p. 273.
65. Hu, H. and R.G. Larson, *Evaporation of a sessile droplet on a substrate.* The Journal of Physical Chemistry B, 2002. **106**(6): p. 1334-1344.
66. Einstein, A., *Investigations on the Theory of the Brownian Movement*. 1956: Courier Corporation.
67. Owens, D.K. and R. Wendt, *Estimation of the surface free energy of polymers.* Journal of applied polymer science, 1969. **13**(8): p. 1741-1747.

68. Wu, S. *Calculation of interfacial tension in polymer systems*. in *Journal of Polymer Science Part C: Polymer Symposia*. 1971. Wiley Online Library.
69. Wu, S., *Polar and nonpolar interactions in adhesion.* The Journal of Adhesion, 1973. **5**(1): p. 39-55.
70. Chun, K.-Y., et al., *Highly conductive, printable and stretchable composite films of carbon nanotubes and silver.* Nature nanotechnology, 2010. **5**(12): p. 853.
71. Yoon, Y., et al., *Highly stretchable and conductive silver nanoparticle embedded graphene flake electrode prepared by In situ dual reduction reaction.* Scientific reports, 2015. **5**: p. 14177.
72. Araki, T., et al., *Printable and stretchable conductive wirings comprising silver flakes and elastomers.* IEEE Electron Device Letters, 2011. **32**(10): p. 1424-1426.
73. Matsuhisa, N., et al., *Printable elastic conductors by in situ formation of silver nanoparticles from silver flakes.* Nat Mater, 2017. **16**(8): p. 834-840.
74. Jin, H., et al., *Enhancing the Performance of Stretchable Conductors for E-Textiles by Controlled Ink Permeation.* Adv Mater, 2017. **29**(21).
75. Hu, M., et al., *Direct pen writing of adhesive particle-free ultrahigh silver salt-loaded composite ink for stretchable circuits.* ACS nano, 2015. **10**(1): p. 396-404.
76. Kumar, A., et al., *A highly deformable conducting traces for printed antennas and interconnects: silver/fluoropolymer composite amalgamated by triethanolamine.* Flexible and Printed Electronics, 2017. **2**(4): p. 045001.
77. Wang, X., Z. Liu, and T. Zhang, *Flexible sensing electronics for wearable/attachable health monitoring.* Small, 2017. **13**(25): p. 1602790.
78. Nishizaki, M. and N. Kobayashi, *Hot-melt solid ink composition*. 2000, Google Patents.
79. Johnson, K.L. and K.L. Johnson, *Contact mechanics*. 1987: Cambridge university press.
80. Wang, Z., A.A. Volinsky, and N.D. Gallant, *Crosslinking effect on polydimethylsiloxane elastic modulus measured by custom‐built compression instrument.* Journal of Applied Polymer Science, 2014. **131**(22).
81. Chilson, L., *The Difference between ABS and PLA for 3D Printing.* ProtoParadigm, Jan, 2013. **26**.
82. Pritchard, R.H., et al., *Precise determination of the Poisson ratio in soft materials with 2D digital image correlation.* Soft Matter, 2013. **9**(26): p. 6037-6045.
83. Torres, J., et al., *Mechanical property optimization of FDM PLA in shear with multiple objectives.* Jom, 2015. **67**(5): p. 1183-1193.
84. Drack, M., et al., *An imperceptible plastic electronic wrap.* Advanced Materials, 2015. **27**(1): p. 34-40.
85. Tybrandt, K. and J. Vörös, *Fast and efficient fabrication of intrinsically stretchable multilayer circuit boards by wax pattern assisted filtration.* small, 2016. **12**(2): p. 180-184.
86. Kim, D.-H., et al., *Epidermal Electronics.* Science, 2011. **333**: p. 838.
87. Chung, H.J., et al., *Stretchable, Multiplexed pH Sensors With Demonstrations on Rabbit and Human Hearts Undergoing Ischemia.* Advanced Healthcare Materials, 2014. **3**(1): p. 59-68.
88. Gao, W., et al., *Fully integrated wearable sensor arrays for multiplexed in situ perspiration analysis.* Nature, 2016. **529**: p. 509.
89. Yokota, T., et al., *Ultraflexible, large-area, physiological temperature sensors for multipoint measurements.* Proc. Natl. Acad. Sci. USA, 2015. **112**: p. 14533.
90. Lipomi, D.J., et al., *Skin-like pressure and strain sensors based on transparent elastic films of carbon nanotubes.* Nature Nanotechnology, 2011. **6**: p. 788-792.
91. Kim, B.-S., et al., *Pattern Transfer Printing of Multiwalled Carbon Nanotube Multilayers and Application in Biosensors.* Chemistry of Materials 2010. **22**(16): p. 4791-4797.
92. Jang, K.-I., et al., *Rugged and breathable forms of stretchable electronics with adherent composite substrates for transcutaneous monitoring.* Nature Communications, 2014. **5**: p. 4779.

93. Cho, G., et al., *Performance Evaluation of Textile-Based Electrodes and Motion Sensors for Smart Clothing.* IEEE Sensors Journal, 2011. **11**(12): p. 3183-3193.
94. Gonçalves, C., et al., *Wearable E-Textile Technologies: A Review on Sensors, Actuators and Control Elements.* Inventions, 2018. **3**(1).
95. Imani, S., et al., *A wearable chemical–electrophysiological hybrid biosensing system for real-time health and fitness monitoring.* Nature Communications, 2016. **7**: p. 11650.
96. Dupont, DuPont PE410 Ink-Jet Silver Conductor Datasheet. **2018 2018.**
97. SNS-NANOFIBER-TECHNOLOGY. *NANOSAN - Sorb*. 2018 [cited 2018 March 28]; Available from: http://www.snsnano.com/pdf/PR-014%20NANOSAN-Sorb%20Technical%20Data%20Sheet.pdf.
98. Sigma-Aldrich. *Ag-flake*. 2018 [cited 2018 June]; Available from: https://www.sigmaaldrich.com/catalog/product/aldrich/327077?lang=en&region=CA.
99. Sigma-Aldrich. *Ag-powder*. 2018 [cited 2018 June]; Available from: https://www.sigmaaldrich.com/catalog/product/aldrich/327085?lang=en&region=CA.
100. Adão, M.H., B. Saramago, and A.C. Fernandes, *Estimation of the surface tension components of thiodiglycol.* Langmuir, 1998. **14**(15): p. 4198-4203.
101. Farina, D., R. Merletti, and R.M. Enoka, *The extraction of neural strategies from the surface EMG.* Journal of applied physiology, 2004. **96**(4): p. 1486-1495.
102. Stoppa, M. and A. Chiolerio, *Wearable electronics and smart textiles: a critical review.* Sensors (Basel), 2014. **14**(7): p. 11957-92.
103. Quandt, B.M., et al., *Body-monitoring with photonic textiles: a reflective heartbeat sensor based on polymer optical fibres.* Journal of The Royal Society Interface, 2017. **14**(128): p. 20170060.
104. Coyle, S., et al., *Textile sensor glove for health monitoring–Application in home assessment of Rheumatoid Arthritis.* Health, 2017.
105. Jerkovic, I., V. Koncar, and A.M. Grancaric, Sensors, 2017. **17**(10): p. 2297.
106. Huang, Y., et al., *Weavable, conductive yarn-based NiCo//Zn textile battery with high energy density and rate capability.* ACS nano, 2017. **11**(9): p. 8953-8961.
107. Xu, S., et al., *Textile Inspired Lithium–Oxygen Battery Cathode with Decoupled Oxygen and Electrolyte Pathways.* Advanced Materials, 2018. **30**(4): p. 1704907.
108. Shi, X., N. Zhu, and G. Zheng, *The combined effect of temperature, relative humidity and work intensity on human strain in hot and humid environments.* Building and environment, 2013. **69**: p. 72-80.
109. Reddy, A., et al., *Fully printed flexible humidity sensor.* Procedia Engineering, 2011. **25**: p. 120-123.
110. Barroca, N., et al., *Wireless sensor networks for temperature and humidity monitoring within concrete structures.* Construction and Building Materials, 2013. **40**: p. 1156-1166.
111. Liu, M., et al., *Large‐Area All‐Textile Pressure Sensors for Monitoring Human Motion and Physiological Signals.* Advanced Materials, 2017. **29**(41): p. 1703700.
112. Pizarro, F., et al., *Easy-to-Build Textile Pressure Sensor.* Sensors, 2018. **18**(4): p. 1190.
113. Raviglione, A., et al., *Real-time smart textile-based system to monitor pressure offloading of diabetic foot ulcers.* Journal of diabetes science and technology, 2017. **11**(5): p. 894-898.
114. Dang, W., et al., *Printable stretchable interconnects.* Flexible and Printed Electronics, 2017. **2**(1): p. 013003.
115. Harris, K., A. Elias, and H.-J. Chung, *Flexible electronics under strain: a review of mechanical characterization and durability enhancement strategies.* Journal of materials science, 2016. **51**(6): p. 2771-2805.
116. Savagatrup, S., et al., *Plasticization of PEDOT: PSS by common additives for mechanically robust organic solar cells and wearable sensors.* Advanced Functional Materials, 2015. **25**(3): p. 427-436.

117. Wang, Y., et al., *A highly stretchable, transparent, and conductive polymer.* Science advances, 2017. **3**(3): p. e1602076.
118. Hirsch, A., et al., *Intrinsically stretchable biphasic (solid–liquid) thin metal films.* Advanced Materials, 2016. **28**(22): p. 4507-4512.
119. Cooper, C.B., et al., *Stretchable capacitive sensors of torsion, strain, and touch using double helix liquid metal fibers.* Advanced Functional Materials, 2017. **27**(20): p. 1605630.
120. Matsuhisa, N., et al., *Printable elastic conductors with a high conductivity for electronic textile applications.* Nat Commun, 2015. **6**: p. 7461.
121. Matsuhisa, N., et al., *Printable elastic conductors with a high conductivity for electronic textile applications.* Nature communications, 2015. **6**: p. ncomms8461.
122. T.-G. La, S.Q., D.K. Scott, R. Bakhtiari, J.W.P. Kuziek, K.E. Mathewson, J. Rieger, H.-J. Chung, *Two-layered and Stretchable e-Textile Patches for Wearable Healthcare Electronics.* Submitted.
123. Hu, L., et al., *Stretchable, porous, and conductive energy textiles.* Nano letters, 2010. **10**(2): p. 708-714.
124. Cui, H.-W., K. Suganuma, and H. Uchida, *Highly stretchable, electrically conductive textiles fabricated from silver nanowires and cupro fabrics using a simple dipping-drying method.* Nano Research, 2015. **8**(5): p. 1604-1614.
125. Lee, H., et al., *Preparation of fabric strain sensor based on graphene for human motion monitoring.* Journal of Materials Science, 2018. **53**(12): p. 9026-9033.
126. Stempien, Z., et al., *In-situ deposition of polyaniline and polypyrrole electroconductive layers on textile surfaces by the reactive ink-jet printing technique.* Synthetic Metals, 2015. **202**: p. 49-62.
127. Liu, L., et al., *Wearable energy-dense and power-dense supercapacitor yarns enabled by scalable graphene–metallic textile composite electrodes.* Nature communications, 2015. **6**: p. 7260.
128. Zahid, M., et al., *Strain-responsive mercerized conductive cotton fabrics based on PEDOT: PSS/graphene.* Materials & Design, 2017. **135**: p. 213-222.